AD-A166 211 ELECTRON-ION RECOMBINATION IN AIR AT EMP FIELDS(U) 1/1
MISSION RESEARCH CORP SAN DIEGO CA
J G CHERVENAK ET AL 12 JUN 85 MRC/SD-R178
UNCLASSIFIED DNA-TR-85-202 DNA001-84-C-0137 F/G 20/4 NL

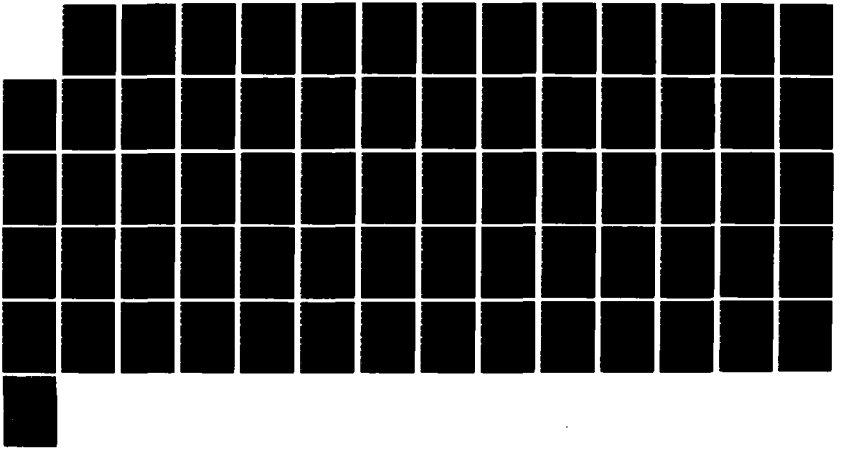

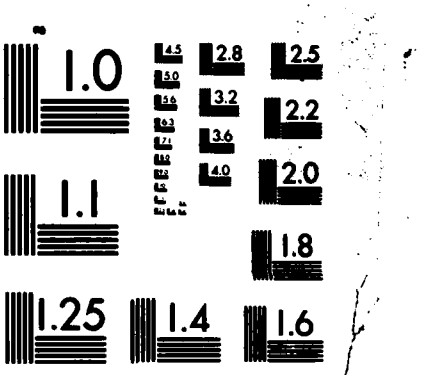

(12)

AD-A166 211

DNA-TR-85-202

ELECTRON-ION RECOMBINATION IN AIR AT EMP FIELDS

J. G. Chervenak
V. A. J. van Lint
Mission Research Corporation, San Diego
5434 Ruffin Road
San Diego, CA 92123-1313

12 June 1985

Technical Report

CONTRACT No. DNA 001-84-C-0137

Approved for public release;
distribution is unlimited.

THIS WORK WAS SPONSORED BY THE DEFENSE NUCLEAR AGENCY
UNDER RDT&E RMSS CODE B326085466 X99QMXVC00013 H2590D.

Prepared for
Director
DEFENSE NUCLEAR AGENCY
Washington, DC 20305-1000

Destroy this report when it is no longer needed. Do not return to sender.

PLEASE NOTIFY THE DEFENSE NUCLEAR AGENCY, ATTN: STTI, WASHINGTON, DC 20305-1000, IF YOUR ADDRESS IS INCORRECT, IF YOU WISH IT DELETED FROM THE DISTRIBUTION LIST, OR IF THE ADDRESSEE IS NO LONGER EMPLOYED BY YOUR ORGANIZATION.

UNCLASSIFIED
SECURITY CLASSIFICATION OF THIS PAGE

AD-A166211

REPORT DOCUMENTATION PAGE

1a. REPORT SECURITY CLASSIFICATION UNCLASSIFIED	1b. RESTRICTIVE MARKINGS
2a. SECURITY CLASSIFICATION AUTHORITY N/A since Unclassified	3. DISTRIBUTION/AVAILABILITY OF REPORT Approved for public release; distribution is unlimited.
2b. DECLASSIFICATION/DOWNGRADING SCHEDULE N/A since Unclassified	
4. PERFORMING ORGANIZATION REPORT NUMBER(S) MRC/SD-R170	5. MONITORING ORGANIZATION REPORT NUMBER(S) DNA-TR-85-202
6a. NAME OF PERFORMING ORGANIZATION Mission Research Corporation, San Diego 6b. OFFICE SYMBOL (If applicable)	7a. NAME OF MONITORING ORGANIZATION Director Defense Nuclear Agency
6c. ADDRESS (City, State, and ZIP Code) 5434 Ruffin Road San Diego, CA 92123-1313	7b. ADDRESS (City, State, and ZIP Code) Washington, DC 20305-1000
8a. NAME OF FUNDING/SPONSORING ORGANIZATION 8b. OFFICE SYMBOL (If applicable)	9. PROCUREMENT INSTRUMENT IDENTIFICATION NUMBER DNA 001-84-C-0137
8c. ADDRESS (City, State, and ZIP Code)	10. SOURCE OF FUNDING NUMBERS PROGRAM ELEMENT NO: 62715H; PROJECT NO: X99QMXV; TASK NO: C; WORK UNIT ACCESSION NO: DH008235

11. TITLE (Include Security Classification)
ELECTRON-ION RECOMBINATION IN AIR AT EMP FIELDS

12. PERSONAL AUTHOR(S)
Chervenak, J.G. and van Lint, V.A.J.

13a. TYPE OF REPORT	13b. TIME COVERED	14. DATE OF REPORT (Year, Month, Day)	15. PAGE COUNT
Technical	FROM 840316 TO 850416	850612	70

16. SUPPLEMENTARY NOTATION
This work was sponsored by the Defense Nuclear Agency under RDT&E RMSS Code B326085466 X99QMXVC00013 H2590D.

17. COSATI CODES		
FIELD	GROUP	SUB-GROUP
20	14	
20	8	

18. SUBJECT TERMS (Continue on reverse if necessary and identify by block number)
EMP
SREMP
Recombination
Electron-Ion Recombination
Air Conductivity

19. ABSTRACT (Continue on reverse if necessary and identify by block number)

A pulsed electron beam and a parallel-plate ion chamber have been used to measure the electron-ion recombination coefficient, β_e, in dry and moist air as a function of the electric field. In moist air the value at 1000 V/cm (10^5 V/m) is in agreement with the value normally used in EMP calculations and results from the agglomeration and clustering of the air ions. An increase in β_e at lower fields is consistent with a recombination process in which H_2^7O molecules act as a third body. The dry air results are a decade below the moist air values at a given field. Direct measurement of the equilibrium field, E_s, was made and found to be consistent with the value expected from the measured recombination coefficient.

The measured values of β_e and E_s show that three-body recombination is not a significant electron removal process at EMP fields.

20. DISTRIBUTION/AVAILABILITY OF ABSTRACT	21. ABSTRACT SECURITY CLASSIFICATION
☐ UNCLASSIFIED/UNLIMITED ☒ SAME AS RPT. ☐ DTIC USERS	UNCLASSIFIED
22a. NAME OF RESPONSIBLE INDIVIDUAL Betty L. Fox	22b. TELEPHONE (Include Area Code) (202) 325-7042
	22c. OFFICE SYMBOL DNA/STTI

DD FORM 1473, 84 MAR
83 APR edition may be used until exhausted
All other editions are obsolete

SECURITY CLASSIFICATION OF THIS PAGE
UNCLASSIFIED

PREFACE

Mission Research Corporation would like to acknowledge the help of the technical staff of the HIFX facility of the Harry Diamond Laboratories for their help in performing this experiment. We especially appreciate the work of Klaus Kerris in supplying and calibrating the special TLD's used here.

CONVERSION TABLE FOR U.S. CUSTOMARY TO METRIC (SI) UNITS OF MEASUREMENT

Multiply	By	To Get
atmosphere (normal)	1.013 E2	kil pascal (kPa)
calorie (thermochemical)	4.184 E0	joule (J)
degree (angle)	1.745 E-2	radian
degree Fahrenheit (°F)	5.556 E-1	degree Centigrade (°C)
electron volt	1.602 E-19	joule (J)
erg	1.000 E-7	Joule (J)
inch	2.540 E-2	meter (m)
micron	1.000 E-6	meter (m)
mil	2.540 E-5	meter (m)
pound (force)/inch^2 (psi)	6.895 E0	kilo pascal (kPa)
rad	1.000 E-2	gray (Gy)
torr (mm Hg, 0°C)	1.333 E-1	kilo pascal (kPa)

TABLE OF CONTENTS

LIST OF ILLUSTRATIONS

SECTION 1
BACKGROUND

In the source region of a nuclear burst an electric field is generated by the outward flux of Compton electrons. This field is limited by the conductivity of the air which is a result of the ionization produced by the Compton electrons. The field builds up until the conduction electrons drift inward at a rate that compensates the outward displaced Compton electrons. This equilibrium field is given by

$$E_s = J_c/\sigma \tag{1}$$

where J_c is the Compton current and σ is the conductivity of the air.

The conductivity, when the motion of the ions are neglected, is given by

$$\sigma = n\, e\, \mu \tag{2}$$

where n is the free electron density and the electron mobility, μ, is a function of E. In general, the electron density depends on the dose rate, $\dot{\gamma}$, the electron attachment rate, α, the ion-ion recombination coefficient, β_i, as well as the electron-ion recombination coefficient, β_e. These parameters are functions of electric field and the water vapor content of the air.

At low $\dot{\gamma}$, n is determined by the attachment rate. In steady state

$$n = \frac{K \dot{\gamma}}{\alpha} \tag{3}$$

where $K = 2.2 \times 10^9$ cm^{-3}/rad is the generation constant in air. Since the dose rate is proportional to the Compton current,

$$J_c = K_c \dot{\gamma} \tag{4}$$

The equilibrium field is then

$$E_s = \frac{K_c \alpha}{K e \mu} \tag{5}$$

which is independent of $\dot{\gamma}$ and is called the saturated field.

At high $\dot{\gamma}$, n is determined by electron-ion recombination. In steady state

$$n = \left(\frac{K \dot{\gamma}}{\beta_e} \right)^{1/2} \tag{6}$$

The equilibrium field is now

$$E_s = \frac{K_c}{e \mu} \left(\frac{\beta_e \dot{\gamma}}{K} \right)^{1/2} \tag{7}$$

Since this field increases with $\dot{\gamma}^{1/2}$, it is not truly saturated. The high dose rate regime is defined by

$$n \beta_e >> \alpha$$

or

$$\dot{\gamma} >> \frac{a^2}{K \beta_e} \tag{8}$$

An initial value of $\beta_e \approx 2 \times 10^{-7}$ cm^3/s, which is due to two-body recombination with N_2^+ and O_2^+, has been measured at low pressure mainly using drift tubes. The value of β_e increases during the pulse as ions form agglomerates like N_3^+, N_4^+ as well as clusters with water molecules. In a typical calculation β_e will reach a plateau value of $\approx 1 \times 10^{-6}$ cm^3/s for moist air (Ref. 5). Recently there has been theoretical and experimental work on another mechanism which is possible when complex molecules like H_2O, CO_2, NH_3, etc., are present in large densities to act as a third body in the recombination process.

1.1 TWO- AND THREE-BODY RECOMBINATION.

The free electrons in a gas follow random paths caused by elastic collisions with the gas molecules. If an electron approaches to within some sphere around a positive ion there will be an attractive force between them. The radius of this sphere is usually taken to be when the electrostatic energy is equal to the average kinetic energy of the electrons, that is

$$r_o = \frac{e^2}{4 \pi \varepsilon_o kT} \tag{9}$$

Recombination may still not occur. The probability of various recombination mechanisms (radiative, dissociative, or dielectronic) are given by the quantum mechanical cross sections. The two-body process can be represented as

$$e + A^+ \xrightarrow{\beta 2} A \tag{10}$$

where β_2 is the two-body rate constant. Increasing the gas density does not affect β_2 since the motion is already random, and a collision is as likely to lead to the escape of the electron as to the capture.

If electrons can undergo inelastic collisions with neutral gas molecules, then three-body recombination can taken place. This can be represented as

$$e + A^+ + M \xrightarrow{\beta_3} A + M^* \qquad (11)$$

where β_3 is the three-body rate constant. At low pressure the rate of this process is directly proportional to the density of the third body because the probability of recombination is greatly increased if the electron loses a large fraction of its kinetic energy while at a radius less than r_o. At high pressure (often near 1 atm) the process saturates and recombination becomes controlled by the electron mobility (or diffusion constant). The total recombination coefficient (below saturation by the third body) is

$$\beta_e = \beta_2 + \beta_3 N \qquad (12)$$

where N is the number density of the third body. When the third body is a non-polar molecule like CO_2, vibrational excitation is the important inelastic process, but for polar molecules like H_2O, rotational excitation dominates.

1.2 PREVIOUS MEASUREMENTS.

Microwave absorption methods have been used to measure a number of two- and three-body recombination rates (Ref. 8). Measurements in pure water vapor up to 20 Torr at 21°C and 81°C (Ref. 6) were used to deduce

$$\beta_2 = 4.1 \times 10^{-6} \text{ cm}^3/\text{s}$$
$$\beta_3 = 2.3 \times 10^{-18} T^{-2.0\pm0.5} \text{ cm}^6/\text{s} \quad (13)$$

From the three-body theory it is not expected that the type of ion would be important in determining β_3, so the value measured for pure water should be applicable to moist air using the H_2O number density for N.

1.3 FIELD DEPENDENCE.

However, the measurement of β_3 was performed at essentially zero electric field, while the β_3 of interest to EMP predictions might be ≈1 kV/cm. Fields of this size heat the electrons to a few tenths of an eV. The dependence of β_3 on gas temperature given above is primarily a reflection of the dependence of β_3 on the electron temperature. The three-body rate constant is expected to go as r_o^3 (Ref. 6), and Equation (9) shows that r_o^3 decreases as the temperature of the electrons increases. Let us assume that the T^{-2} dependence, derived by changing T by 21%, holds over an electron temperature increase of a factor of four to 0.1 eV. Then β_3 would be at least a factor of 16 smaller than that found above and β_e would not be much larger than the two body rate.

The only previous measurement of a three-body electron-ion recombination rate made at a non-zero field was performed on CO_2 (Ref. 4). Here it was found that the three-body rate fell very rapidly with electric field while the two-body rate fell only very slowly.

SECTION 2
EXPERIMENT DESIGN

Although the dose to the air in a nuclear blast is initiated by the prompt and delayed gamma rays, it is the Compton electrons that produce the free electron-ion pairs that cause the air to be conducting. In order to reach the high dose rate regime, where recombination is the dominant free electron removal mechanism, in an above ground test, it is necessary to use an electron beam directly from a simulator.

As we have seen, the measurement of the electron-ion recombination coefficient must be performed at realistic fields in order to be relevant to EMP. This can be done with a parallel-plate ion chamber. The essential idea of the experiment then becomes:

1. Apply an electric field to the gas in the ion chamber.

2. Shoot a pulse of high energy electrons through the chamber to produce a large density of electron-ion pairs.

3. Measure the ion chamber current during the pulse to infer the electron density.

4. Calculate β_e using previously measured air properties (e.g., electron mobility and attachment).

2.1 THE ELECTRON BEAM.

HIFX (flash x-ray machine at Harry Diamond Laboratories) was used as the electron beam generator. With a 4.1 MV charge, HIFX produces a fairly narrow distribution of electron energies with a peak at 2.4 MeV and a maximum energy of 3.0 MeV. The beam is transported in a 6" diameter pipe of variable length and pressure. Extremely high dose rates can occur when conditions are such as to produce a beam pinch. Under more stable conditions it is possible to produce dose rates of 10^{14} rad/s. Most of the data reported here is for a dose rate of 4×10^{13} to 10^{14} rad/s at the entrance to the ion chamber. At HIFX energies, the value of K_c in Equation (4) is 5.9×10^{-12} $(A/cm^2)/(rad/s)$, so beam current density was as large as 600 A/cm^2.

If we use a nominal value of $\alpha = 10^8$ s^{-1} and a minimum value of 2×10^{-6} cm^3/s for β_e in Equation (8) we find that recombination dominates over attachment for dose rates large compared to 2×10^{12} rad/s. Thus the HIFX dose rates are quite adequate for studying recombination.

The shape of the HIFX beam current waveform varied extensively from shot to shot. The FWHM varied from 10 to 20 ns but was usually around 16 ns. The rise time was also variable and the pulse often rose in two or more steps. At a dose rate of 5×10^{13} rad/s for a time of 10 ns, 10^{15} cm^{-3} free electrons are generated in the air. Later it will be shown that the equilibrium electron densities were on the order of 10^{14} cm^{-3}, so that by the peak of the HIFX pulse there is sufficient time for the electron density to grow to the point that it is controlled by recombination.

2.1.1 Beam Transport.

If a high current electron beam is injected into a vacuum, the strong electrostatic repulsion will cause the beam to "blow up". Only if a gas is used to produce a background of positive ions can the repulsive force be reduced enough that it is balanced by the inward force of the beam's

self-magnetic field. Such a "charge neutralized" beam can then be propagated down a conducting drift tube with the return current flowing on the tube's inner surface. If the gas density is too high, the magnetic force will cause the beam to constrict and a pinch may occur.

In some electron beams (especially those of large ν/γ, see below) there is also a tendency for the beam to be "current neutralized". Because of the changing flux associated with the beam's current the return current tends to flow as close to the beam current as possible. When the conductivity of the gas is large enough most of the return current can be carried by the gas, reducing the inductance of the beam plus return path.

A critical parameter in the transport of intense, relativistic electron beams is called ν/γ (Ref. 2). γ is the usual relativistic measure of a particle's energy in units of its rest energy. ν measures the "linear density" of a beam and, as such, is a measure of the electrostatic repulsion. ν is defined as the number of electrons per cm^3 times the classical electron radius. The ratio ν/γ is then a measure of the "stiffness" of the beam; the smaller ν/γ, the stiffer the beam and the easier to get the beam to propagate. It has been shown that ν/γ must be less than one for a beam to propagate without an external magnetic field.

The HIFX beam has $\gamma = 5.7$. The maximum current output is 20 kA. This gives a maximum value of ν/γ of 0.2, so the HIFX beam is quite stiff and easy to propagate with the proper background pressure. When the beam is passed through a collimator, ν is reduced, and the beam passing into the ion chamber has a ν/γ of only 0.02.

Two configuations were used in this experiment. In the first, the outer chamber that housed the ion chamber was mounted to the end of the drift tube, and the beam passed directly from the partial pressure of the drift tube, through a 2-mil Al foil window, into the collimator and ion

chamber containing 1 atm of air. In the second configuration, the chamber was separated from the drift tube, which consisted only of the 10-cm pumping section. The 1 1/4" air gap between the 2-mil Ti window on the drift tube and the chamber window was surrounded by a 1 1/8" Cu pipe. Four Cu strips connected from the chamber to the drift tube. Dosimetry results presented later show that the additional air gap introduced a significant divergence to the beam as it passed through the ion chamber. Presumably this was due to a pinching (and then a spreading) of the beam in the air gap or to a perturbation of the beam return current, since the effect was too large to be explained on the basis of additional scattering in the Ti window and air.

In the course of the experiment it was found that the best procedure was to operate the drift tube close to high vacuum conditions and vary the length of the tube to vary the dose. The dose at the end of a fixed length of drift tube could be increased by increasing the pressure in the tube, but this caused very sharply peaked pulses which make the data very difficult to analyze.

2.1.2 Charge Neutralization.

The charge injected into the chamber by the beam would produce very large fields if the beam were not neutralized. For example, if the beam was 1 cm in radius and carried 500 A/cm^2, the longitudinal electric field at the edge of a 1 cm slice of the beam would be

$$\begin{aligned} E &= \frac{1}{2}\,\frac{\rho}{\epsilon_0}\,d \\ &= \frac{1}{2}\,\frac{J}{\nu\epsilon_0}\,d \\ &= 95\ \text{kV/cm} \end{aligned} \qquad (14)$$

This is also the value of the radial E field at the edge of the beam.

If the electron density in the gas is 10^{14} cm^{-3} the conductivity is about 0.02 S/cm. The charge relaxation time is then

$$\tau = \varepsilon_0/\sigma \qquad (15)$$
$$= 5 \text{ ps}$$

So if the rise time of the pulse is 5 ns, the fields reach only values close to 100 V/cm. If this slice of beam lies between the center and ground electrodes of the ion chamber, neither the radial or longitudinal fields are directed such as to drive current across the gap of the ion chamber. The effect of the charge carried by the beam was observed in the voltage measuring grids in the chamber and will be discussed further under the data analysis.

2.1.3 Back emf of the Beam.

As mentioned above, the circuit consisting of the beam and return current path has an inductance. A change in the beam current produces a back, longitudinal electric field that does drive current in the air between the plates of the ion chamber. The inductance has two components: one due to magnetic flux in the beam and one due to the flux that lies between the beam and the return path. The current density is approximately constant over the cross section of the beam. The back emf varies across the beam, being a maximum at the center and zero at the surface of the return path.

In Figure 1 the dashed line shows the path to which we apply Faraday's Law.

$$\oint E_c \cdot d\ell = \frac{d}{dt} \int B \cdot dA$$

$$E_c \ell = \frac{\mu_0 \dot{I} \ell}{2\pi} \frac{1}{r_0^2} \left[\int_0^{r_0} r \, dr + \int_{r_0}^{a} \frac{1}{r} \, dr \right]$$

$$E_c = \frac{\mu_0 I}{2\pi} \left(\frac{1}{2} + \ell n \frac{a}{r_0} \right) \qquad (16)$$

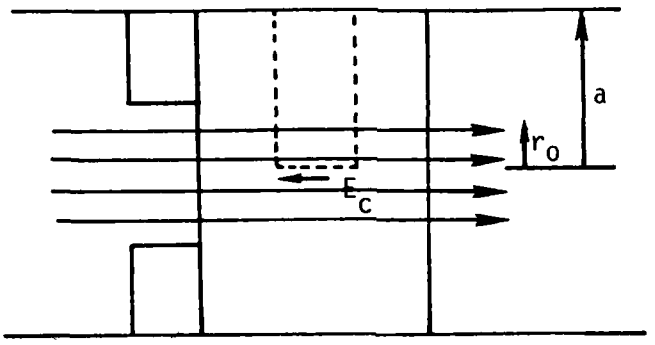

Figure 1. A back emf is produced by a change in the current of the e-beam.

This is the maximum field which occurs on the axis of the beam. When averaged over the cross-sectional area of the beam, the field is

$$E = \frac{\mu_0 \dot{I}}{2\pi}\left(\frac{1}{4} + \ell n\ \frac{a}{r_0}\right) \tag{17}$$

In order to keep E small, a should be kept small. That is, the chamber must be designed so that the beam return current flows as close to the beam as possible. In our case, r_0 = 1 cm, a = 3 cm, $\dot{I} \approx 10^{11}$ A/s. This gives E = 140 V/cm. This is a small effect at fields of prime interest to EMP (1000 V/cm) but could affect measurement at lower applied fields. The effect of this field is reduced because the ion chamber used here is a double-sided chamber. Since the back field is direct along the beam, in one half of the chamber it adds to the applied field while in the other half it subtracts. A smaller compensating effect is due to the fact that as the electric field increases, the electron mobility decreases.

The back emf that has just been calculated is the force that causes electron beams to become current neutralized. The backward driven plasma current in the ion chamber is

$$J = \sigma E$$
$$= 3\ A/cm^2$$

Since this is negligible compared to the beam current density, the HIFX beam is not current neutralized in the ion chamber, and a Rogowski coil can be used to measure the beam current.

2.2 THE CHAMBER.

An outer chamber was made to serve as the vacuum container for either of two ion chambers with different electrode spacings or an equilibrium field diode (to be discussed below). A scale drawing of this chamber is shown in Figure 2.

The chamber was made to seal to the end of the drift tube. A 1/2" Al plate backed by a 1/8" Pb sheet was mounted on the front of the chamber with Al bolts to serve as a stopping block for the beam that did not enter the chamber. An internal collimator, with a 3/4" diameter hole consisted of two pieces: one also acted as a clamp ring to hold the front window and the other as a housing for the Rogowski coil. The thickness of the Rogowski coil housing was varied to accomodate the different thickness ion chambers.

The chamber was vacuum tight and bakeable to greater than 200°C in order to remove all water vapor before filling with dry air. Due consideration was taken of thermal expansion. In particular, the outer area of the backplate was made 1/8" thick in order to flex at high temperature.

There were two 2-mil Al foil windows. The front window separated the partial pressure of the drift tube from the vacuum or atmospheric pressure of the chamber. The window behind the ion chamber separated the chamber air from the beam diagnostics which were located in the room air. Both windows were held in place by clamping the foils against Viton O-rings.

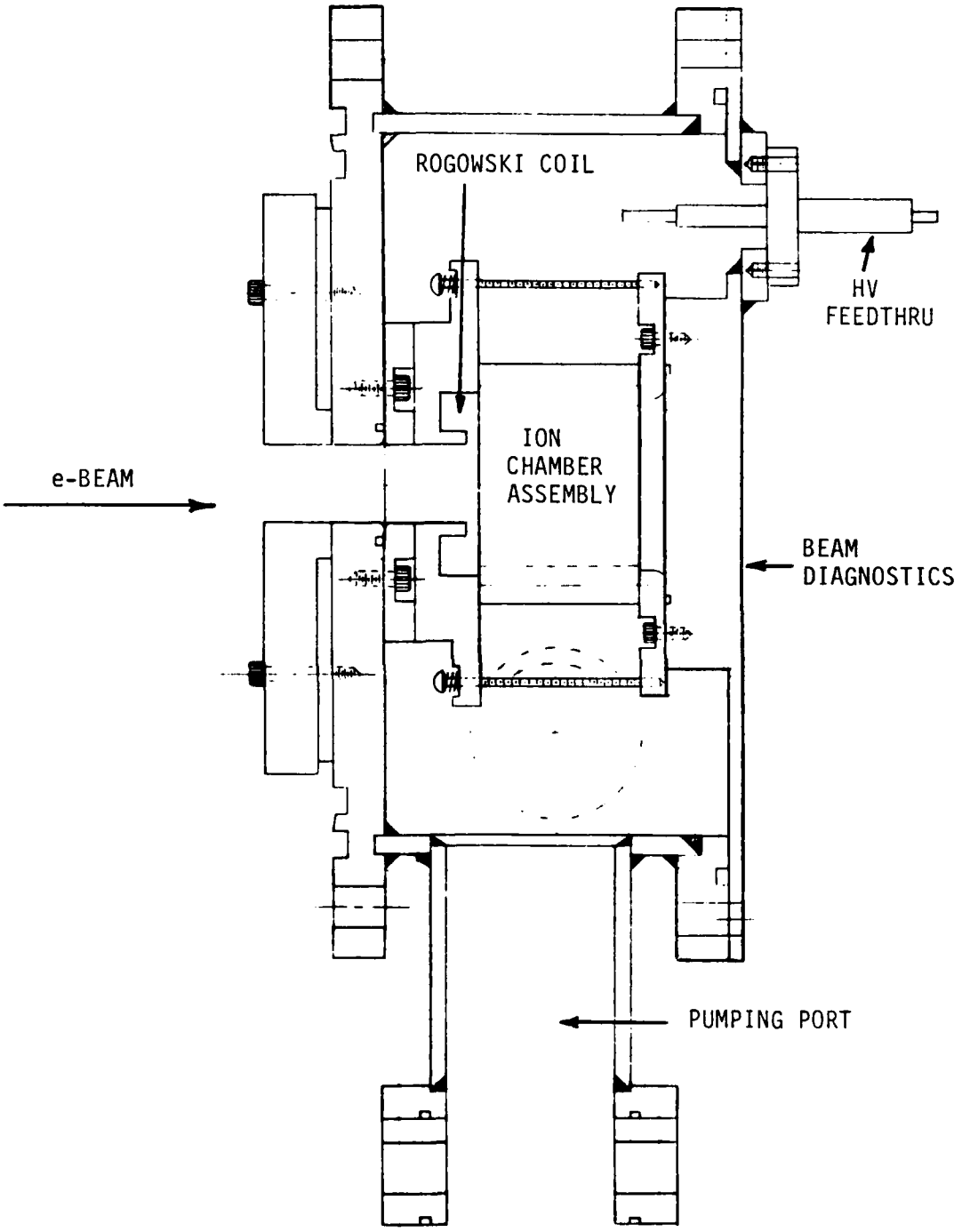

Figure 2. Vacuum chamber that housed either of two ion chambers or the equilibrium field diode.

There was one high voltage feedthrough and six SMA vacuum feedthroughs mounted in the backplate.

The signals were carried on Cujac cables from a junction box mounted on the rear of the chamber to a second junction box where they were joined to RG-223 cables. These cables ran in high quality (low transfer impedance) conduit to the screen room. The Cujac cables were shielded from stray bremsstrahlung radiation with a layer of lead bricks. The conduit was connected to the screen room and then carried inside and connected to a patch box in an equipment rack. The cables in the conduit connected to panel feedthroughs on the front of the box, and RG-58 cables were then connected from the patch panel to the various recording devices. The most important of the data were recorded on a Tektronix 7912 AD transient digitizer, often with two signals recorded sequentially. The other fast signals were recorded on Tektronix 7844 oscilloscopes.

2.2.1 Air Samples.

The chamber was baked at 120°C for 1 hour while under diffusion pump vacuum. When the temperature returned to that of the room, the pressure read 2×10^{-5} Torr. The chamber was then filled with commercial dry air to a pressure of 1 atm. Although the chamber was originally designed to measure the water content of the air from IR absorption, the wet air data was obtained on air saturated with water vapor. The chamber was filled with water vapor from a reservoir and then filled to 1 atm with room air which already had an 80% or greater relative humidity. The excess water condensed on the internal chamber surfaces, and the air remained saturated at the chamber's temperature during the experiment. The chamber temperature was measured with a calibrated thermistor.

2.2.2 Ion Chambers.

The ion chamber is shown schematically in Figure 3. The ion chamber is double-sided with a center electrode and two ground electrodes of 1 mil Al foil. There are two voltage measuring grids made from 90% transparent, 5 mil, Al wire mesh. The electrodes and grids were separated with teflon spacers. Two spacings were used: 3/16" for the "1/2 cm" chamber and 3/8" for the "1 cm" chamber. In order to reduce the inductance, the chamber measuring resistor was made up of about 40 parallel resistor placed radially outward from the center electrode. Also the storage capacitor was a large number of parallel capacitors placed around the periphery of the ion chamber. Both chambers had a capacitance of 0.032 μF. The "1/2 cm" chamber had a resistance of 3.40 Ω and the "1 cm" chamber had a resistance of 3.18 Ω.

The ion chamber capacitors also serve as the return path for the beam current. During the course of the experiment an oscillation occurred in the ion chamber current for very fast rising pulses. Ten-ohm resistors were inserted into the ground leads of one set of capacitors, in order to put some damping resistance into the circuit consisting of beam inductance and storage capacitance. Also a Cu foil was wrapped over the outside of the capacitors to confine any leakage flux. This served to effectively remove the oscillations.

2.2.3 Scattering.

The electrons passing through the foils and grids of the ion chamber undergo multiple Coulomb scattering. The divergence of the beam is increased as it passes through each window and electrode. If we assume that there is effectively 4 mil of Al at the front of the chamber, then the rms scattering angle is 8°, and the beam area is increased by about 30% at the rear of the chamber. The divergence of the beam was measured and accounted for in the data analysis.

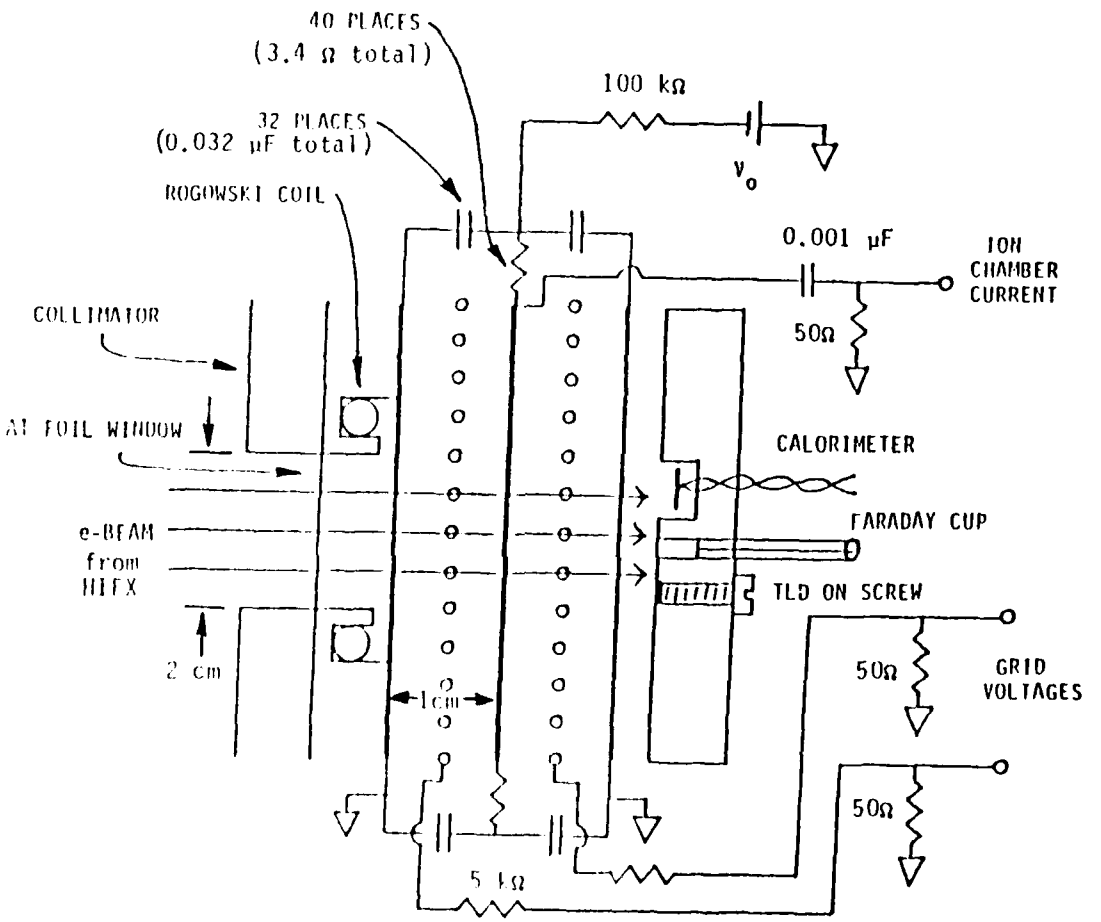

Figure 3. Schematic diagram of the ion chamber measurement.

2.2.4 Boundary Layer.

Very large densities of electrons and ions are created in this experiment. When the electrons drift under the motion of the applied field, a layer of positive ions are left behind at the cathode. The potential can quickly appear across the boundary layer rather than the bulk of the gas. As an example let us assume that the ions are immobile, $n = 10^{14}$ cm^{-3}, $\mu = 10^3$ $cm^2/V \cdot s$, and that 10^3 V are applied to a 1 cm gap. Then in 5 ns the electrons would leave behind a layer of positive ions 5×10^{-3} cm thick with a voltage of more than 2×10^3 V across it. Since this is more than the available voltage, there would be no field on the bulk of the gas.

In the above example, as the electric field builds in the boundary layer, the ion current to the cathode increases. Since the ion mobility is about 10^3 times smaller than the electron mobility, the field in the boundary layer will greatly exceed that in the bulk of the gas before the ion current to the cathode can match the electron current in the bulk. Often the electron avalanche field will be exceeded in the boundary layer. There are then a number of processes that determine the boundary layer voltage:

1. Ions in the boundary layer drift to the cathode.

2. A small fraction ($\approx$0.001) of the ions cause electrons to be emitted upon impact.

3. The emitted electrons, as well as free electrons produced by the radiation, avalanche in the boundary layer.

4. This increases the ion density, decreases the thickness of the boundary layer, and reduces the boundary layer voltage.

A detailed, computer calcuation is necessary to predict the boundary layer voltage.

In this experiment grids were used to measure the electric field in the bulk of the gas. The center electrode was usually operated at a negative voltage and the voltage from grid to ground (anode) does not include the voltage on the boundary layer.

2.2.5 Grids.

The Debye shielding length is given by

$$\lambda_d(\text{cm}) = 7.0 \left(\frac{T(^\circ K)}{n(\text{cm}^{-3})} \right)^{1/2} \tag{18}$$

In the fields applied during this experiment the electrons are heated to tenths of an eV. Equation (18) then gives a Debye length on the order of 10^{-5} to 10^{-4} cm. Since this is much smaller than any of the physical dimensions of the ion chamber, the ionized air in this experiment must be treated as a plasma.

The voltage measuring grids are really probes immersed in the plasma. The Debye length is much smaller than the spacing between the grid wires, and each wire acts independently. The constraints on the grids are then:

1. The grids must be placed along an equipotential.

2. The grids must be sufficiently transparent to not impede the current.

3. The grids must remain close to the plasma potential.

The grid circuit used for the data taken during this experiment is shown in Figure 4.

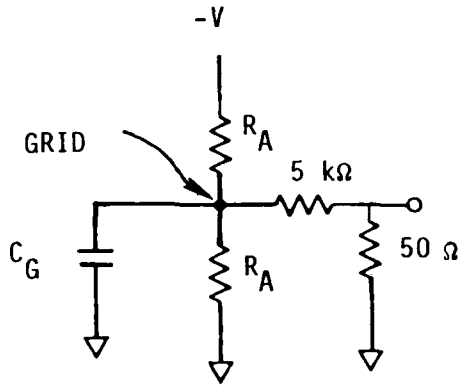

Figure 4. Grid circuit.

R_A is the resistance of the air, C_G is the capacitance of the grid to ground, and -V is the voltage on the bulk of the air. Grid current is drawn through both the resistive divider and the stray capacitance. If the plasma potential at the grid is 500 V, the resistor carries 100 mA. The stray capacitance of the grid to ground is about 10 pF. If the grid is required to charge to the 500 V in 1 ns, then the current drawn by the capcitance is 5 A, much larger than the resistor's current.

This current must be furnished by the plasma. The random electron current available in the plasma is

$$J_e = n\, e\, \bar{v}_e$$

$$= n\, e \left(\frac{k\, T_e}{2\pi m_e} \right)^{1/2} \tag{19}$$

$$\approx 270 \text{ A/cm}^2$$

The random positive ion current is less, both because the ion mass is much larger and because the ion temperature is thermal.

$$J_i = N_+ e \left(\frac{kT_i}{2\pi m_i}\right)^{1/2} \tag{20}$$

$$= 0.2 \text{ A/cm}^2$$

The grid has a surface area in the plasma of 2.85 cm^2 x 0.1 x π, or 0.9 cm^2. The electron current is initially much larger than the ion current and much larger than the current carried to ground by the grid. After the grid's capacitance has been charged, the potential of the grid adjusts negatively with respect to the plasma to a value which cuts the electron current such that

$$I_e - I_i = 100 \text{ mA}$$

If we assume that the electron distribution is still Maxwellian, despite the heating by the field,

$$0.3 \text{ A} = 270 \text{ A/cm}^2 \times 0.9 \text{ cm}^2 \times e^{-\frac{eV}{kT}}$$

and V = 7 V. So the grid is driven only slightly below the plasma potential at the grid's location.

2.3 THE MEASURING CIRCUIT.

There were very stringent design requirements placed on the experiment by the measuring circuit. The logical flow is as follows:

1. The large amount of ionization produces a very low air resistance in the chamber, ≈2 Ω.

2. The measuring resistor, between the center electrode and the storage capacitor must be on he order of the air resistance or most of the applied voltage appears on the measuring resistor instead of the chamber.

3. But the measuring resistor also serves as the damping resistor in the circuit consisting of the chamber capacitance, the storage capacitor, and the wiring inductance.

4. Thus to prevent oscillations the inductance in the measuring circuit must be held to a minimum.

As an example, we estimate the capacitance of the chamber to be 10 pF and the inductance of a wire running to a resistor and storage capacitor eternal to the chamber to be 100 nH. The frequency of oscillation is then 150 MHz, and the critical damping resistance is 200 Ω. Either the circuit will oscillate with a small measuring resistor or almost no voltage will be across the chamber with a large measuring resistor. It is therefore necessary to locate the resistor and capacitor inside the vacuum chamber and to distribute them, as described above, in order to reduce the inductance.

If the inductance was reduced to 0.1 nH, then the critical damping resistance would be 6 Ω. A compromise value of ≈3 Ω was used. The circuit is sufficiently damped, and only about one half of the applied voltages is lost.

2.3.1 Circuit Analysis.

The circuit used to measure the ion chamber current is shown in Figure 5.

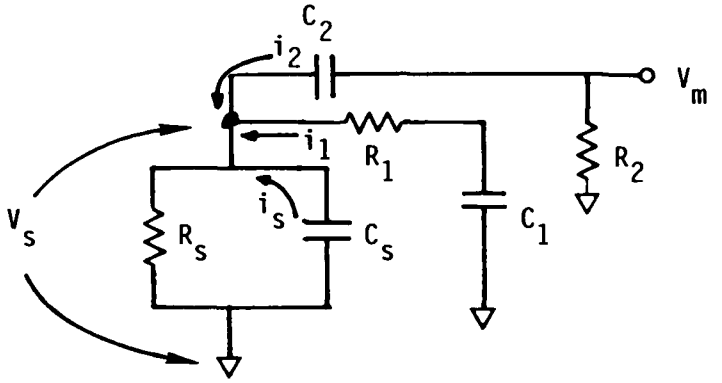

C_1 = storage capacitor = 0.032 μF
C_2 = coupling capacitor = 0.001 μF
C_S = air sample capacitance ≈ 10 pF
R_1 = measuring resistor = 3.4 Ω
R_2 = terminating resistor = 50 Ω
R_S = air sample resistance ≈ 2 Ω
V_S = sample (chamber) voltage
V_m = measured voltage

Figure 5. Measuring circuit.

Not shown on the diagram is the voltage source used to initially charge all capacitors to V_m; the power supply is resistively isolated from the circuit on the time scale of interest. Also not shown is a voltage monitor circuit used to verify that a voltage of V_o appeared at the chamber. $V_m(t)$ was recorded and we wish to infer $I(t) = i_1 + i_2 + i_S$, the total current flowing through the air in the chamber.

Before presenting the exact equations, it is of value to think of the circuit in terms of three time constants. A change in the air resistance causes the voltage across the chamber to change with

$$\tau_1 = (R_1 \,||\, R_S) \times (C_1 \,||\, C_S) \qquad (21)$$
$$\approx 3\ \Omega \times 10\ \text{pF}$$
$$\approx 30\ \text{ps}$$

where the || symbol is used to represent the reciprocal of the sum of the reciprocals of two numbers. This time constant shows that V(t) will closely follow $R_S(t)$. The measured voltage is related to V_S by a time-constant differentiation with a time constant of

$$\tau_2 = R_2 C_2 = 50 \text{ ns} \tag{22}$$

Since the HIFX pulse had a FWHM of 20 ns, a small, but not negligible, decay occurs on V_m when V_S is unchanged. The third time constant controls the sag of the applied voltage

$$\tau_3 \approx (R_1 + R_S) \times C_1 = 170 \text{ ns} \tag{23}$$

This is quite long compared to the 20 ns HIFX pulse, so the voltage applied to the resistor combination of R_1 and R_S stays constant at V_o.

If we do not include the time constant effects, then the equations are

$$\begin{aligned} V_S &= V_o + V_m \\ i_1 &= -V_m/R_1 \\ i_2 &= -V_m/R_2 \\ i_S &= -C_S \frac{dV_m}{dt} \end{aligned} \tag{24}$$

The current i_S is always small (less than 1%) compared to i_1, especially since measurements are made where $V_m(t)$ is not changing rapidly. The total current is then

$$I(t) = -V_m(t)/(R_1 \,||\, R_2) \tag{25}$$

The exact equations, including the time constants, are

$$V_S(t) = V_o + V_m(t) + \frac{1}{R_2C_2} \int_o^t V_m(t')\, dt'$$

$$I(t) = -V_m(t)/R_2 - V_s(t)/R_1 \qquad (26)$$

$$+ \frac{1}{R_1} e^{-t/R_1C_1} \left[V_o + \frac{1}{R_1C_1} \int_o^t e^{t'/R_1C_1} V_S(t')\, dt' \right]$$

This leads to ≈10% corrections to the above equations for our typical data.

2.4 BEAM DIAGNOSTICS.

Linear processes, such as attachment, can be measured from the total dose and the integral of the ion chamber current. Recombination is a nonlinear process and requires for its determination that the current and dose rate be known at a particular time. Thus it is very important in this experiment to measure accurately both the dose and waveform.

The beam diagnostics used during this experiment were:

1. A Rogowski coil that meaured the derivative of the beam current, $\dot{I}_b$, at the entrance to the ion chamber. When numerically integrated this gives the dose rate as a function of time, $\dot{\gamma}(t)$.

2. Faraday cups that measured $I_b(t)$, or $\dot{\gamma}(t)$, at the rear of the chamber.

3. Thin Cu foil calorimeter that measured total dose at the rear of the chamber.

4. TLD's that measured total dose at the rear of the chamber.

The last three of the diagnostics were located in the backplate of the chamber, which served as a stopping block for the beam. A thin foil served as a window so that the diagnostics could be in the room air. This allowed easy access to the TLD's without disturbing the air sample and removed the requirement for a vacuum feedthrough for the thermocouple on the calorimeter.

2.4.1 Rogowski Coil.

The Rogowski coil was used as an $\dot{I}$ measuring device to avoid circuit oscillations that can occur when the usual low value shunt resistor is used. The coil consisted of a simple torus of teflon insulated wire wound on a teflon core. The area of a turn was ≈ 0.4 cm^2 and there were about 8 turns. The Rogowski coil was mounted in a housing that served as the final length of the collimator in front of the ion chamber. The diameter of the torus was 1 3/8".

It can be shown that a changing current passing through the hole of the torus produces a voltage source in the coil that is, to first order, independent of position of the current and is given by $K\dot{I}$ where

$$K = \frac{\mu_o n A}{S} \tag{27}$$

Here n is the number of turns, A is the area of a turn, and S is the circumference of the torus. The equivalent circuit is shown in Figure 6. The inductance of the Rogowski coil is

$$L = \frac{\mu_o n^2 A}{S} \tag{28}$$

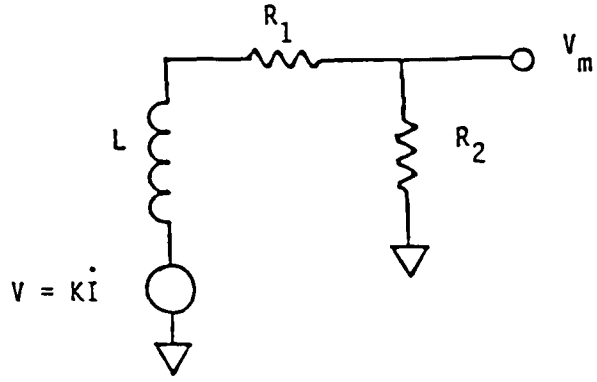

Figure 6. Rogowski coil equivalent circuit.

Solving the circuit for I, we find

$$I(t) = \frac{R_1 + R_2}{KR_2} \int_0^t V_m(t')dt' + \frac{L}{KR_2} V_m(t) \qquad (29)$$

Using the values given above we find that K = 3.7 nH, L = 30 nH and

$$I(t) = 0.54 \int_0^t V_m(t')dt' + 0.16\, V_m(t)$$

where t must be expressed in ns. At the peak of the pulse the integral of V_m is at least 10 times larger than V_m and the second term is small in comparison to the first. The second term represents high frequency components that are lost in the integration.

The Rogowski coils were calibrated by running a square pulse of current through them on a wire. A coaxial ground, short length of wire, and terminating plate with 50-Ω resistor were needed to preserve the risetime of the pulse. Figures 7 to 9 show the calibration pulse, the Rogowski coil

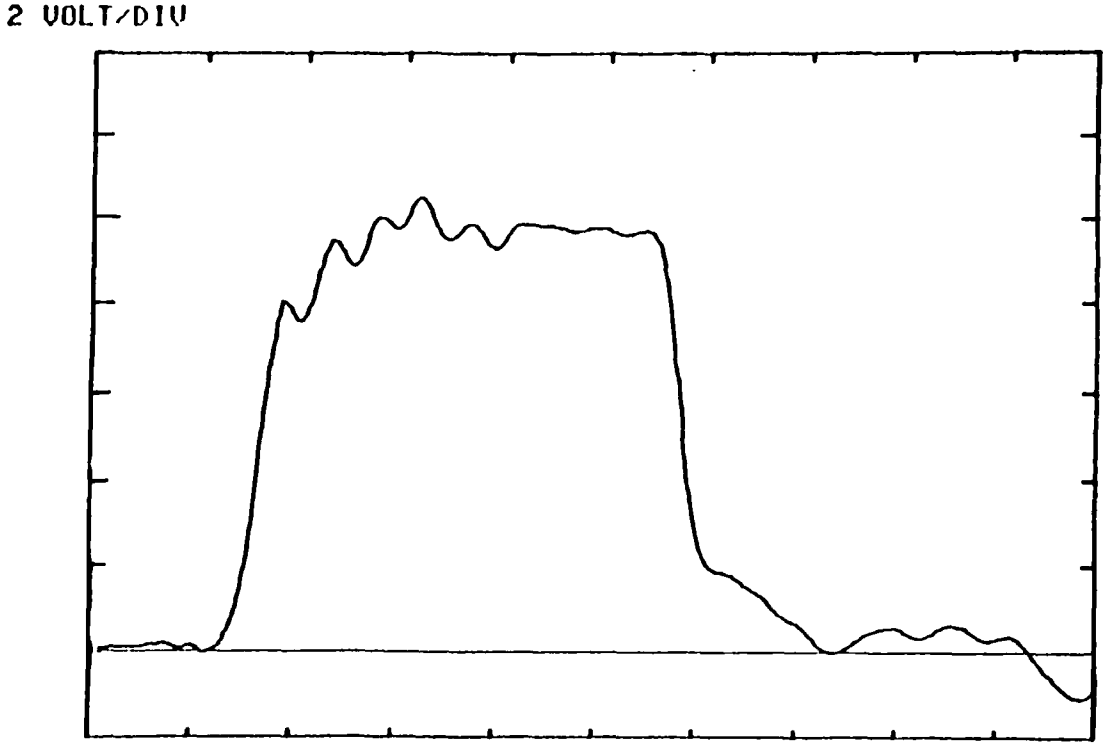

Figure 7. Calibration pulse for Rogowski coil.

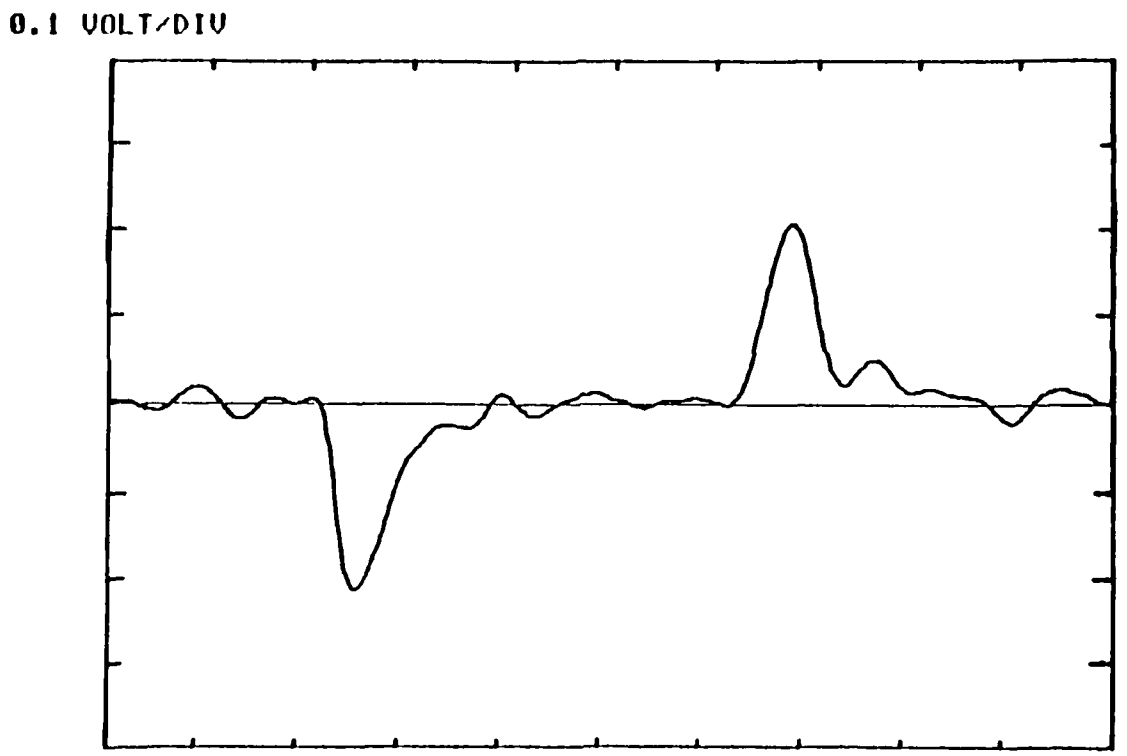

Figure 8. Rogowski coil output waveform.

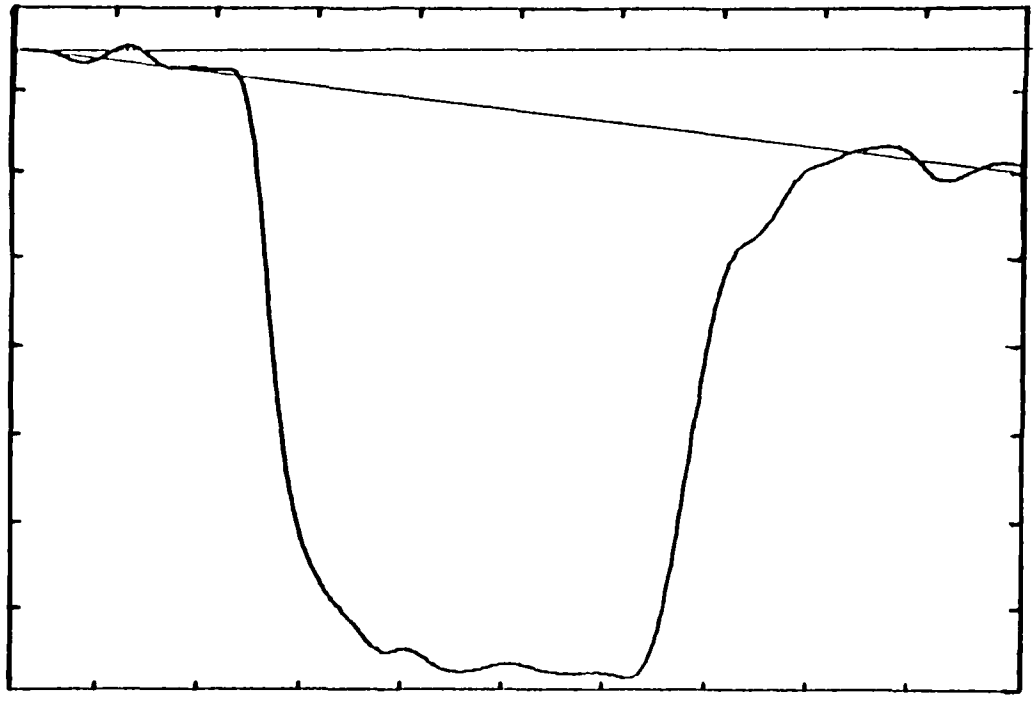

Figure 9. Numerical integration of Rogowski coil. A slight baseline shift in the Rogowski coil waveform causes the baseline of the integrated waveform to be slanted this was taken into account in the calibration procedure.

waveform, and the integral of the Rogowski coil. Note that the rise and fall times of the reconstructed pulse are very close to those of the input pulse but that the high frequency wiggles on the top of the pulse are not as pronounced. An improvement could be made by adding in part of the un-integrated waveform as in the second term in Equation (29), but it was not judged to be necessary for the purpose of this experiment. Very accurate waveforms of the HIFX current are obtained with the Faraday cups. Using just the integral, the coefficient of the first term in Equation (29) was found to be 0.36, 0.40, 0.41 A/V·ns for the three, nominally identical Rogowski coils used here.

2.4.2 Faraday Cup.

In a corruption of the original meaning, any device used to stop an electron beam and measure the current is nowadays called a Faraday cup. It is very difficult to get the inductance low enough to avoid oscillations in a Faraday cup used to stop a large fraction of the beam and shunt it to ground through a low impedance. We have taken the approach of using a 50-Ω cable as the load on the Faraday cup and then choosing the area small enough that the developed voltage is below the breakdown potential of the cabling. The 50 Ω impedance insures efficient damping of the leakage flux caused by non-50 Ω geometry at the cup.

The Faraday cups used here were simple devices fabricated from 0.141 Cujac cable and small Al pellets and were mounted directly in a hole in the back plate of the chamber as shown in Figure 10. The Al pellet was held to the center condcutor of the Cujac by heating the pellet, cooling the wire, and allowing both to come to room temperature after insertion. The pellet was completely wrapped in teflon tape to avoid shorting to the back-plate or foil window. The pellet is more than an electron range thick and the Faraday cups were tested to withstand 500 V. The area of the Faraday cups was typically 0.07 cm^2; a 100 A/cm^2 current at the rear of the chamber would produce a voltage of 350 V. During these experiments voltages up to 800 V were measured without any evidence for breakdown.

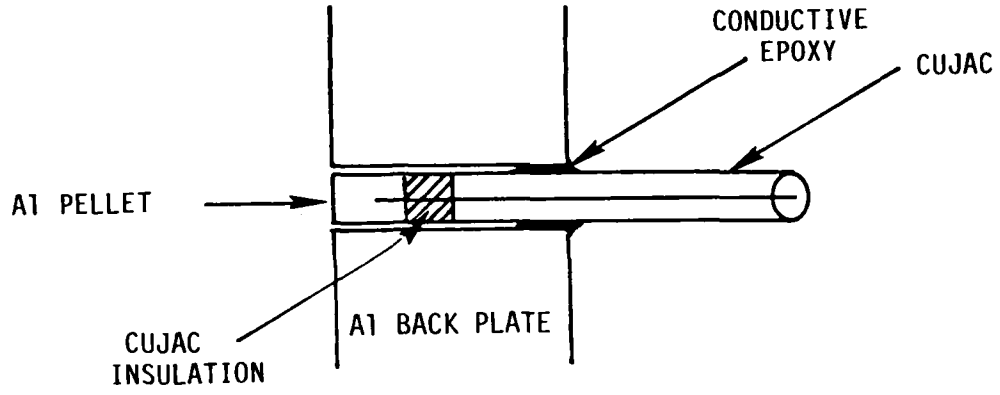

Figure 10. Faraday cup construction. Twice scale.

A calculation showed that the signal due to electrons stopping in the teflon was only about 4% of that due to electrons collected by the Al pellet. This is offset by the loss of charge due to backscattering and secondaries which amounts to about 5%. The capacitance of the Faraday cup can be estimated from the dimensions of Figure 10 to be about 4 pF.

The equivalent circuit of the Faraday cup is shown in Figure 11.

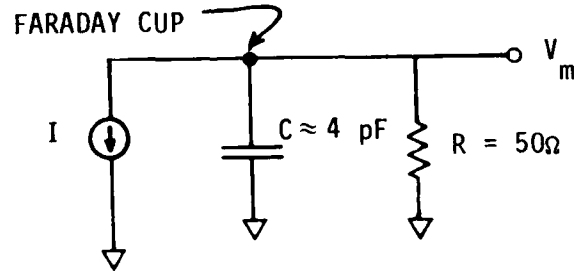

Figure 11. Equivalent circuit of Faraday cup.

The current source of the incident beam causes electrons to flow back to ground through the stray capacitance and terminating resistor. We find

$$I(t) = \frac{V_m(t)}{R} + C\,\frac{dV_m(t)}{dt} = \frac{1}{R}\left(v + \tau\,\frac{dV}{dt}\right) \qquad (30)$$

where τ = 0.2 ns. The Faraday cup measurements were normally used at the peak of the pulse or some other place where dV/dt is small. The second term is normally 2% or less of the first term and was neglected here.

2.4.3 Calorimeter.

The 5 mil thick Cu foil calorimeter is thin compared to the 15 mil average range of 2 MeV electrons in Cu. At 2 MeV the stopping power is a very weak function of the energy. A chromel-alumel thermocouple, with a sensitivity of 40 μV/°C at room temperature, was attached to the foil with a small drop of thermally conducting epoxy. The foil had a diameter of 6 mm, was sandwiched between two styrofoam sheets, and mounted in a hole in the backplate.

The mass of Cu was more than 100 times the mass of the epoxy plus thermocouple leads, so the specific heat of Cu (0.092 cal/gm °C) controlled the temperature rise of the calorimeter. The major source of heat loss from the calorimeter is down the thermocouple leads and a calculation showed a time constant of 6 s. This is in excellent agreement with the value of 11 s found from the semi-log plot of a calorimeter record in Figure 12.

The thermocouple leads ran to a junction box about 2 ft from the beam line where the chromel and alumel wires were connected to the copper wires of a twisted shielded pair (TSP) cable. These connections were made on a massive Cu block to insure that the secondary junctions remained at room temperature. Both sides of the circuit were also capacitively coupled to ground at this point to remove any fast transient introduced by the beam. The TSP cable connected to an operational amplifier in the screen room and then to a Visicorder.

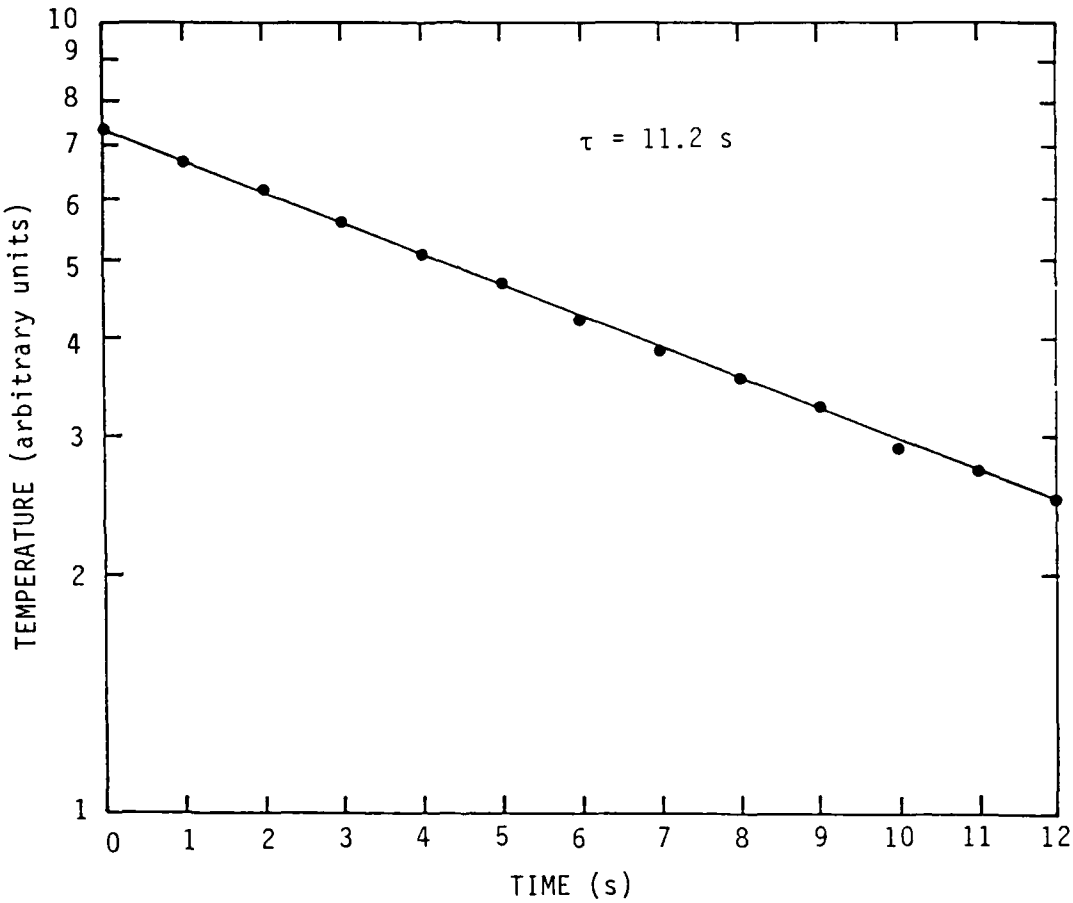

$$\tau = \frac{\Delta t}{\ell n \frac{A_2}{A_1}} = \frac{14 \text{ s}}{\ell n \frac{73}{21}} = 11.2 \text{ s}$$

Figure 12. Measured time constant of the calorimeter is 11 s.

2.4.4 Thermoluminescent Dosimeters.

The dose and dose rates used in this experiment are larger than those encountered in most TLD applications. It was decided to use a TLD composed of 5% CaF_2:Mn powder in a Teflon matrix because there was more data on this material at high dose and high dose rate (Ref. 1) than newer materials that may have superior properties. This material showed no dose rate dependence at 3×10^{11} rad/s from Aurora in the bremsstrahlung mode but starts to saturate at 100 krads total dose.

The available TLD's were 6 mm in diameter and 16 mm thick. In order to map the dose at the rear of the ion chamber the TLD's were punched to a 3 mm diameter. The small TLD's were recalibrated by HDL personnel with a Co^{60} source to 300 krads and were found to scale from the usual TLD calibration curve by the ratio of the mass of the small TLD's to the large TLD's. The TLD's were wrapped in Al foil, glued to an Al screw, and inserted into the backplate from the rear. The TLD's were used on a number of shots as a cross check of the other beam diagnostics, but the shot-to-shot measurement of the dose was made with the calorimeter, Faraday cups and Rogowski coil.

2.4.5 Layout.

The various beam diagnostics, except for the Rogowski coil, were mounted in holes in the backplate of the chamber and distributed in order to check the uniformity of the beam. The pattern is shown in Figure 13.

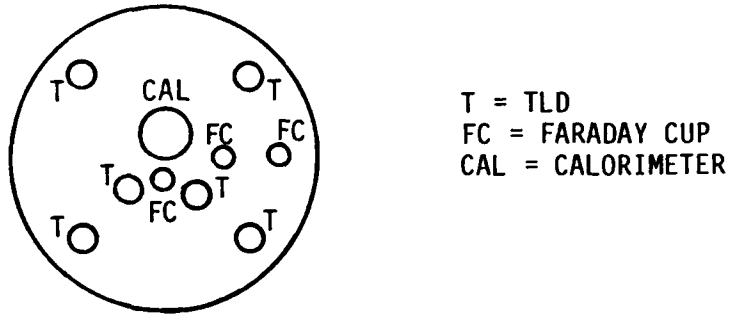

Figure 13. Pattern of beam diagnostics in the chamber backplate.

2.5 THE EQUILIBRIUM FIELD MEASUREMENT.

A check can be made on the electron-ion recombination coefficient mesaured with the ion chamber by directly generating and measuring the equilibrium field. The basic idea of the way that this can be done is shown in Figure 14.

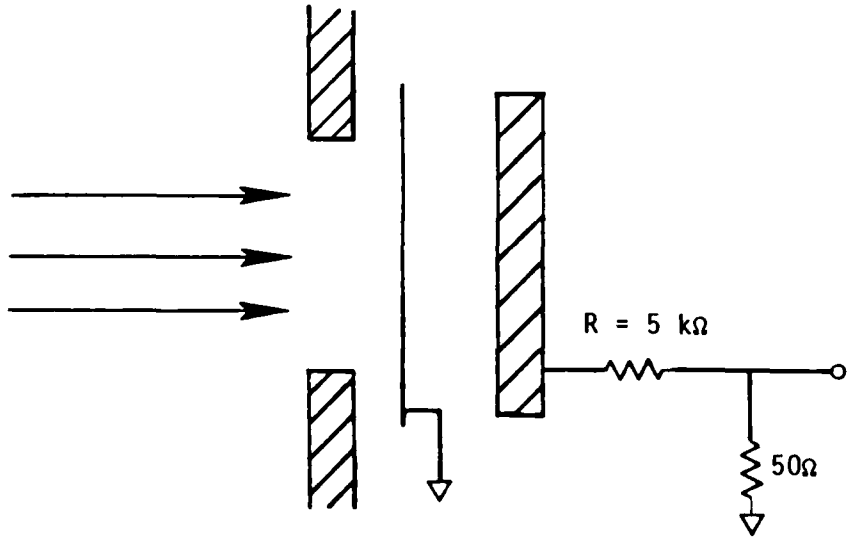

Figure 14. Simplified diagram of measurement of the equilibrium field.

This device, which we refer to as an equilibrium field diode, consists of two electrodes: a thin grounded electrode and a thick high voltage electrode. The electron beam passes through the front electrode but is stopped by the rear electrode. The electron beam serves not only to ionize the air but also to produce a field by charging the thick electrode. As the thick electrode charges and a field builds up in the air, a conduction current carries charge through the air back to the grounded thin electrode.

The potential of the thick electrode approaches the equilibrium voltage according to

$$V_S = R_A I_b \, (1 - e^{-t/R_A C}) \tag{31}$$

where R_A is the resistance of the air and C is the capacitance between thick and thin electrodes. If the dimensions are similar to those of the ion chamber, the air resistance will be $\approx 2\ \Omega$ at the highest dose rate and C ≈ 10 pF. This shows that the current drawn through the measuring voltage divider will be negligible compared to the current through the air and that the steady state voltage, V_S, is attained with a very short time constant, ≈0.2 ns.

As with the ion chamber a boundary layer will form at the thick electrode and its potential will be larger than that given by Equation (31). This can again be avoided by measuring the voltage to the thin electrode from a grid inserted between the two electrodes.

2.5.1 Matching K_c.

The equilibrium field diode, as described so far, would not measure the equilibrium field generated by a nuclear burst. This is because the value of K_c in Equation (4) is larger for a parallel beam of electrons

than for the divergent flux of Compton electrons produced by gamma rays. Since the air would be receiving a smaller dose rate for the same current density the fields in the equilibrium field diode would be larger. For γ rays, $K_c \approx 2.5 \times 10^{-12}$ (A/cm^2)/(rad/s), whereas for HIFX, $K_c \approx 5.9 \times 10^{-12}$ (A/cm^2)/(rad/s). The equilibrium fields from gammas and from an electron beam differ by even more than the ratio of the K_c's because of the electric field dependence of the electron mobility. The equilibrium field diode was compensated in this experiment for this effect by making the thick electrode transmitting over part of its area and adding a second ground electrode as in Figure 15.

A sector hole was cut in the center electrode, but the hole is covered on both sides by 1 mil Al foils. Only part of the beam now acts to charge the thick electrode, and an additional air resistance is introduced in the rear of the diode. The size of the hole is chosen to make the field the same as that from gamma rays. The steady state electric field is given by

$$E_s = R_A I_b / d \tag{32}$$

where d is the spacing between electrodes. Allowing for an area of beam stopping (A_1) different from the area of the resistor (A_2) we have

$$E_s = \frac{Jb}{\sigma} \frac{A_1}{A_2}$$

$$= \sqrt{\frac{\beta\dot{\gamma}}{K}} \frac{K_c}{e\mu} \frac{A_1}{A_2} \tag{33}$$

We call the fraction of the area of the thick electrode that is transparent to the beam η. Then $A = (1 - \eta) A$ and $A = (1 + \eta)A$, where A is the area of the beam. Equation (33) becomes

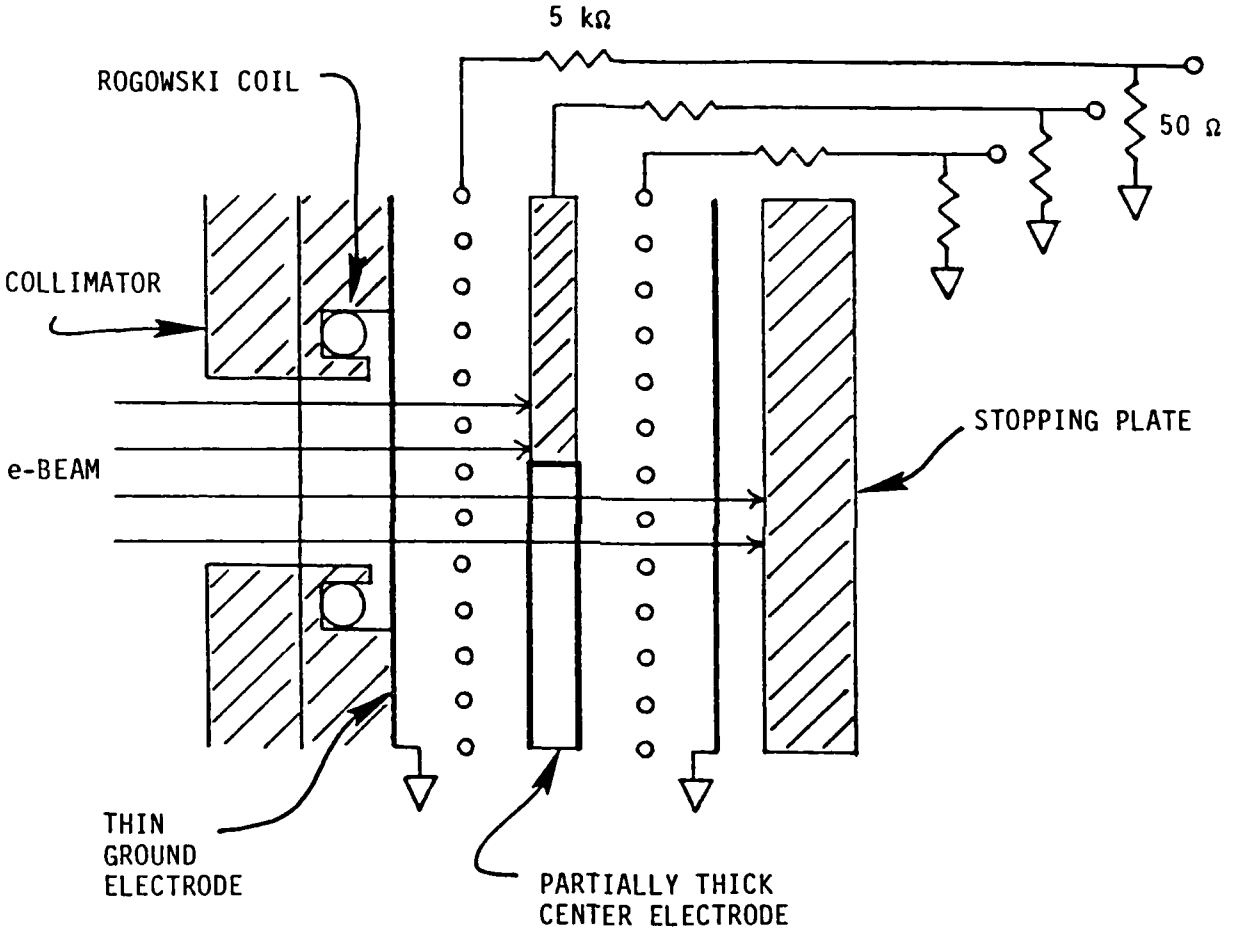

Figure 15. Schematic diagram of the equilibrium field measurement.

$$E_s = \sqrt{\frac{\beta\dot{\gamma}}{K}} \quad \frac{K_c}{e\mu} \quad \frac{1 - n}{1 + n} \tag{34}$$

Since K_c for HIFX electrons is 2.4 times too large, we chose n = 0.42 (angle of sector hole = 150°) to make the diode produce the same fields that would be produced by gamma rays.

The whole equilibrium field diode assembly was covered by a cylinder rolled from a sheet of Cu foil with holes for the center electrode and grid leads. This cylinder served as the return current path for the beam, keeping any back emf small compared to the voltage developed in the diode. The diode was mounted in place of the ion chamber in the vacuum chamber (See Figure 2). With the center electrode partially transmitting, the beam diagnostics in the backplate could be used.

2.5.2 Elevated Gas Temperature.

The recombination process with water molecules acting as a third body depends upon the loss of energy by the electron to the rotational levels of the H_2O molecule. We have seen that there is theoretical and experimental evidence to suspect that the value of β_e depends strongly on the temperature of the electrons. A somewhat heuristic extention of the Thomson theory of three-body recombination (Ref. 6) led to the expression

$$\beta_3 = 5.7 \times 10^{-9} \left(\frac{\nu_\mu}{N}\right) T^{-3} \ (cm^6/s) \tag{35}$$

where ν_μ/N is the energy exchange rate coefficient and can be found from electron swarm data. In this derivation the electron temperature is taken as the gas temperature, T.

Since the spacing of the rotation energy levels in asymmetric top molecules like H_2O are on the order of 10^{-3} to 10^{-4} eV (Ref. 3), the distribution of the H_2O molecules among the rotational levels can be changed by modest changes in gas temperature. Thus there is a possibility that besides the dependence of β_3 on electron temperature there is also a dependence on neutral gas temperature through the ν_μ/N factor in Equation (35). The equilibrium field diode was designed to operate at room temperature and at a temperature of 200°C. At the fields generated in the diode, the electron temperature is determined by the field, and a large change in the steady state voltage can be attributed to the dependence of β_3 on gas temperature. Due account must be taken for other temperature dependent quantities such as the electron mobility.

A thermistor was epoxied into a hole in the Rogowski coil housing and monitored in the screen room during high temperature operation of the equilibrium field diode.

SECTION 3
DATA ANALYSIS

3.1 DOSIMETRY.

Two configurations were used to transport the electron beam into the chamber. In the first arrangement the vacuum chamber was mounted on the end of the drift tube and only a 2 mil Al window separated the drift tube partial pressure from the atmospheric pressure of the chamber. The dose calculated from an integration of the Faraday cup, the calorimeter, and the TLD's agreed to within 10%. The dose obtained from a double integration of the Rogowski coil was a factor of 40% larger, which is consistent with a calculation of the scattering of the electron beam in the foils and grids in the chamber.

In the second configuration, there was a 3-cm air gap between the end of the beam tube and the vacuum chamber. The calorimeter now measured 40% larger than the central Faraday cup, and the Rogowski coil was found to give a dose 1.82 ± 0.15 times that of the calorimeter on 27 shots for which the Rogowski coil signal was manually digitized and doubly integrated. This second configuration is the one that was used for the high dose-rate data from which the electron-ion recombination coefficient was found.

In analyzing the data the chamber was divided into a front half with the dose rate given by the Rogowski coil and a back half with the dose rate scaled to the calorimeter. The dose-times-area product was kept constant in keeping with the assumption that beam spreading was responsible for the fall-off in the dose.

3.2 GRID SIGNALS.

The voltage signal measured by the grid has many potential sources:

1. The applied voltage.

2. Drop in applied voltage to the air as the chamber draws current through the chamber load resistance.

3. Magnetic coupling to the beam.

4. Charge in transit through the chamber.

The first three of these have already been treated.

The beam that traverses the chamber is neutralized by plasma electrons that are driven to the walls. however, there is a time constant of $\tau = \varepsilon_0/\sigma$ needed to relax charge injected into the chamber by a change in the beam current. For the initial rise of the current there is an additional time required to build up the conductivity in the air. Once there is sufficient conductivity, the rate equation for the net charge in the chamber is

$$d\rho = \frac{1}{c}\frac{dJ}{dt}\,dt - \nabla\cdot\sigma E\,dt \qquad (36)$$

where J/c is the charge density in the beam. Rearranging,

$$d\rho = \frac{1}{c}\dot{J}\,dt - \sigma\frac{\rho}{\varepsilon_0}\,dt$$

$$= \frac{1}{c}\dot{J}\,dt - \frac{1}{\tau}\rho\,dt$$

If τ is much less than the time interval over which J changes, the quasi-steady state solution for ρ is

$$\rho = \frac{\tau \dot{J}}{c} \tag{37}$$

Since the grid will see a potential proportional to ρ, it will have a component that goes as the derivative of the beam current.

In Figure 16a is shown a grid voltage signal produced on a shot with $V_o = 0$. The peaks and valleys can be associated with similar features in the derivative of the beam current given by Rogowski coil signal of Figure 16b. In the example following Equation (14) we estimated τ to be 5 ps and found that a field on the order of 100 V/cm would be produced. This is of the same size as the field measured in Figure 16a.

The largest uncertainty in this experiment is the voltage on the air as measured by the grids. The quality of the grid signal increased as the applied voltage increased. This is because the component of grid voltage due to charge injected into the chamber decreases in relative importance and in absolute value as the air conductivity is increased at higher field. Figure 17 shows that at an applied voltage of ≈4 kV, the grid voltage could be determined quite accurately.

3.3 STOPPING CURRENT.

Charge from the beam that stops in the air, grids, and foils of the chamber will produce signals even when the applied voltage is zero as shown by Figure 18. These stopping currents carry charge from ground to grid and center electrode and can be included in the circuit as in the diagram of Figure 19. $I^S_{C.E.}$ is the stopping current to the center electrode, I^S_G is the stopping current to the grid, R_A is the resistance of the air, and $R_{B.L.}$ is the resistance of the boundary layer. The node equations lead to

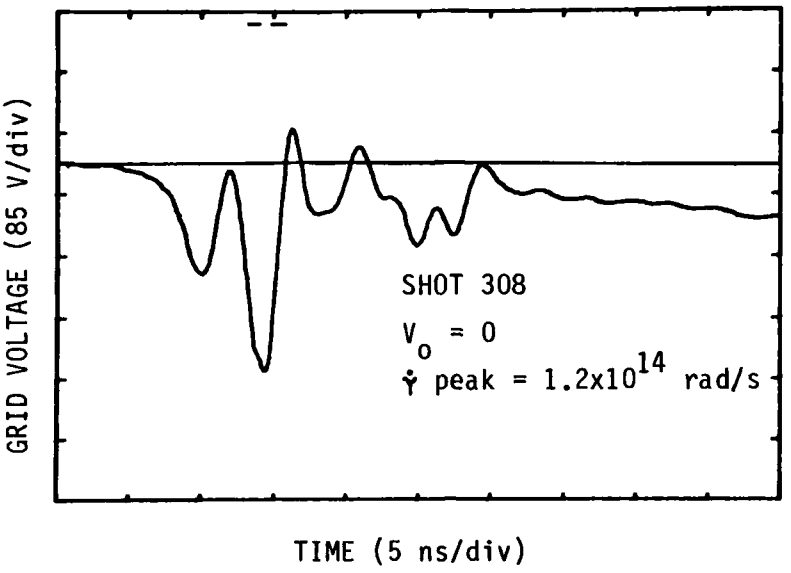

(a)

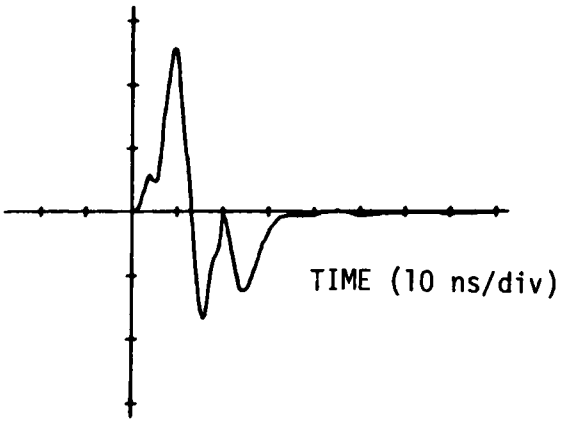

(b)

Figure 16. Grid voltage (a) and Rogowski coil (b) waveforms on a low applied voltage shot.

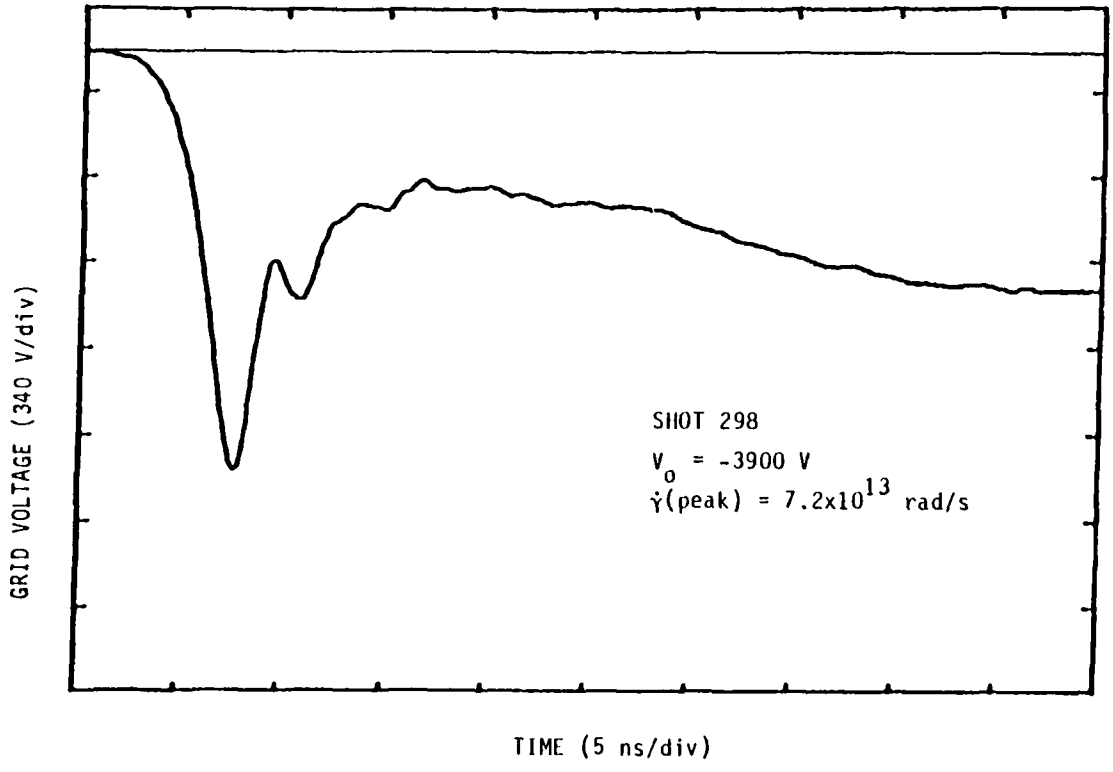

Figure 17. Grid voltage on a shot with a large applied voltage.

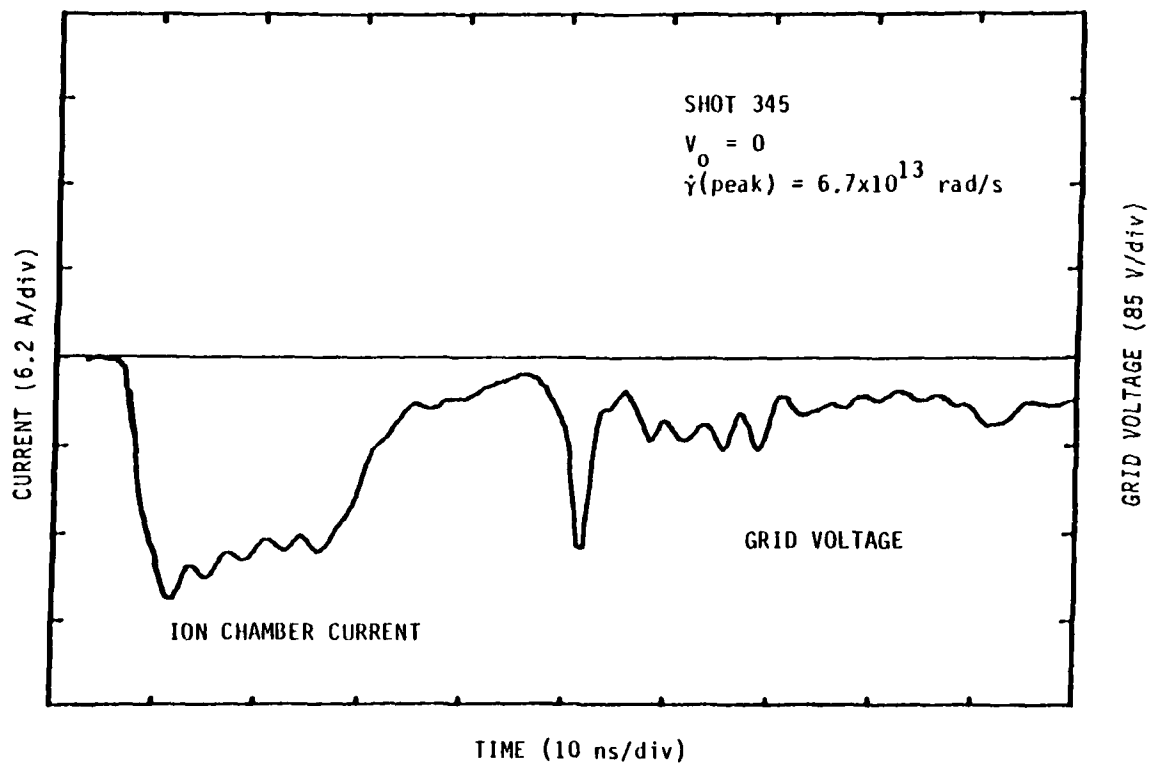

Figure 18. Signals produced by beam stopping currents.

$$-(V_m/R_L) - I^S_{C.E.} - I^S_G - (V_G/R_A) = 0 \tag{38}$$

Assume

$$I^S_{C.E.} + I^S_G = K^S\dot{\gamma} \tag{39}$$

Then for a $V_o = 0$ shot we can find K^S from .

$$K^S = (-V_m/R_L - V_G/R_A)/\dot{\gamma} \tag{40}$$

Once we know K^S the corrected current through the air is

$$I_A = (V_m/R_L) + K^S\dot{\gamma} \tag{41}$$

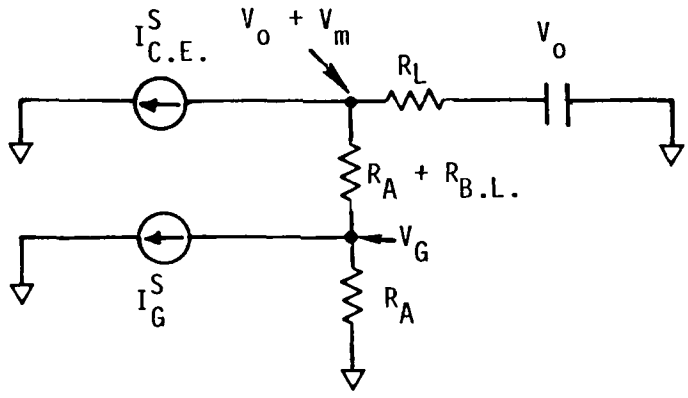

Figure 19. Ion chamber circuit with stopping currents included.

One problem in finding K^S from Equation (40) is that it requires the air resistance, which is not know a priori. After an initial guess at R_A, the data was analyzed and a value for β_e was found. The data was then analyzed a second time using the value of R_A in Equation (40) from the first value found for β_e. The grid voltage trace shown in Figure 18 is the best voltage record obtained on a $V_0 = 0$ shot (because of the smooth beam current waveform). Using this voltage, the recorded value of $\dot{\gamma}$, and the field dependent values of μ, α, and β_e, we find an air resistance of $\approx$3.5 Ω and from Equation (40) a value of 4.6×10^{-13} A/(rad/s) for K^S. The ion chamber current was then corrected according to

$$I_A = V_m/R_L + 4.6 \times 10^{-13} \dot{\gamma} \tag{42}$$

where $\dot{\gamma}$ is measured by the Rogowski coil.

If one uses the rule of thumb that the fraction of beam electrons stopped in a material is equal to the material's thickness expressed as a fraction of the electron range, the value of K^S estimated for the grid, center electrode foil, and air in the chamber is $\approx 6 \times 10^{-13}$ A/(rad/s), in good agreement with the value found above.

3.4 THE ELECTRON-ION RECOMBINATION COEFFICIENT.

We assume that the electron density in the ion chamber is in a quasi-steady state, that is, that the characteristic time for a change in dose rate is long compared to the relaxation time of the electron density ($\tau \approx 1/\alpha + 1/\beta_e n$). If the dose is uniform throughout a volume,

$$n = I/e\mu EA \tag{43}$$

and

$$\beta_e = \frac{2(K\dot{\gamma} \mp \alpha n)}{n^2 \left(1 + \sqrt{1 + 4\,\frac{\alpha}{n\beta_i}}\right)} \qquad (44)$$

In order to take into account two regions with different dose rates we used the following procedure:

1. Guess n_1.
2. Calculate $n_2 = 1/A_2(I/e\mu E - n_1 A_1/A_2)$.
3. Generate β_e^1 and β_e^2 from Equation (44).
4. Iterate until $\beta_e^1 = \beta_e^2$.

Previously measured, field-dependent values of μ and α were used (Ref. 7).

The graph of Figure 20 shows the resulting electron-ion recombination coefficient as a function of electric field over the range that could be attained in the ion chamber. The moist air data appears to be approaching the expected three-body value ($\approx 1.7 \times 10^{-5}$ cm^3/s) at low field. At fields of interest to EMP ($\approx$1000 V/cm), however, β_e has fallen to $\approx 1 \times 10^{-6}$ cm^3/s, a value consistent with clustered two-body recombination, only. The dry air data are about a factor of ten below the moist air at 300 V/cm where the data overlap. The dry air data spans a range of electric field lower than that of the moist air. This is because the decreased values of β_e correspond to larger chamber currents and thus more voltage dropped across the chamber load resistor.

The error bars in Figure 20 were based on fixed uncertainties of 10% for μ, α, and $\dot{\gamma}$, 5% for A, and 100% for β_i. However, the error bars are really determined by the uncertainties in the chamber current and voltage.

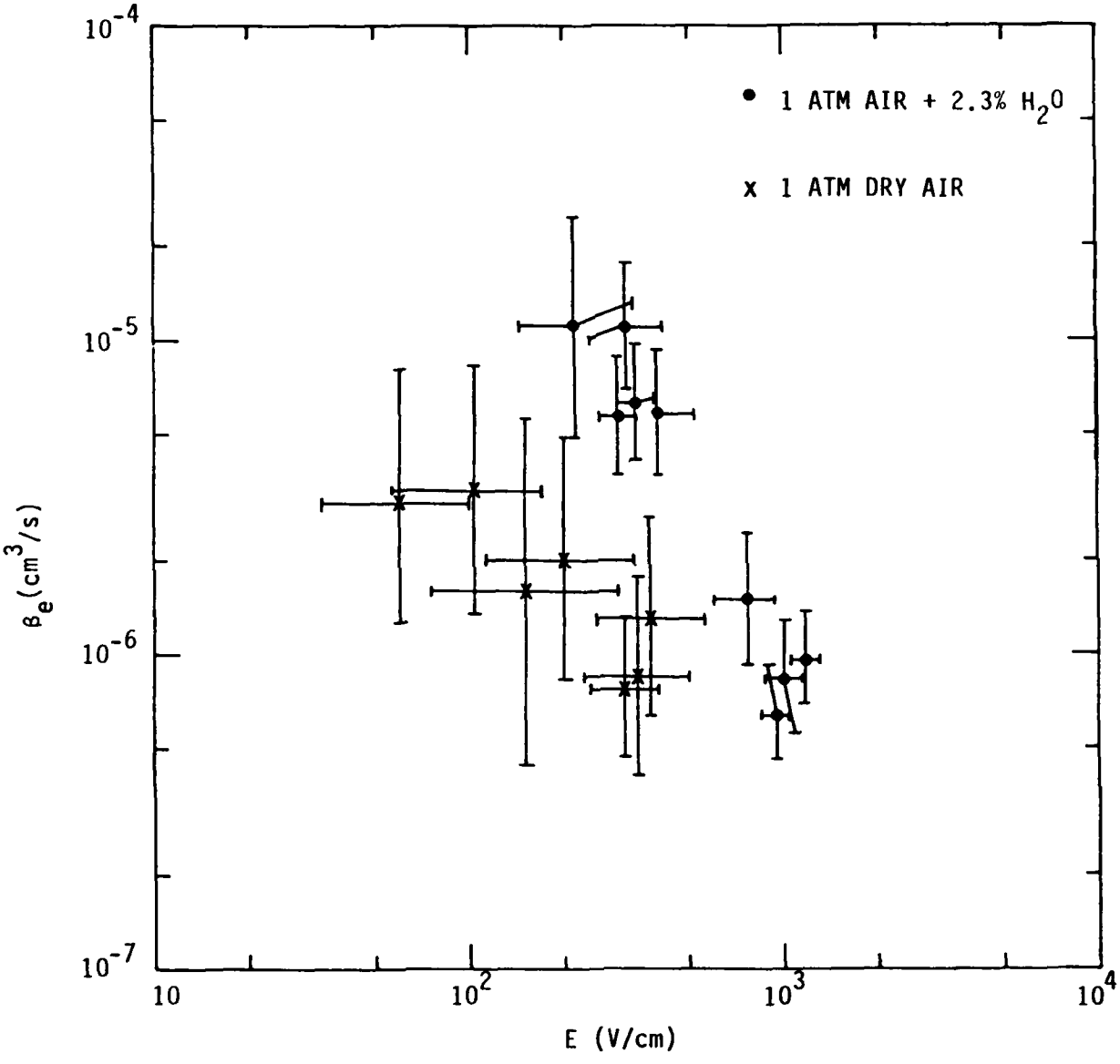

Figure 20. The electron-ion recombination coefficient in dry and moist air.

The uncertainty in the current was taken to be 10% of the uncorrected current plus 30% of the correction. The uncertainty in the voltage varied from shot to shot depending on the shape of the individual dose-rate waveform and applied voltage; values varied from 10 to 100%.

Some data were taken in addition to that shown in Figure 20. The ion chamber with the 2 cm spacing was used extensively in trying to get data at lower fields. Unfortunately, the divergence of the electron beam was such that some beam electrons stopped in the teflon spacers, making very large zero voltage signals. Some data were taken at lower dose rates, $\approx 10^{12}$ rad/s. These data verified the expected value of α to within about 10%, but it is not possible to obtain accurate recombination information, because recombination is responsible only for about 10% of the free electron removal.

3.5 THE EQUILIBRIUM FIELD.

The equilibrium field diode was also exposed in the two configurations: when mounted on the end of the 60-cm drift tube the entrance dose rate was $\approx 2 \times 10^{12}$ rad/s, when mounted separate from the 10 cm drift tube the dose rate was $\approx 5 \times 10^{13}$ rad/s. The grid voltage was again very uncertain because of noise due to charge injected into the chamber. One of the best grid voltage records is shown in Figure 21a; a much more uncertain voltage signal is shown in the second signal in Figure 21b.

Table 1 lists the values of the field for the high and low exposure, for moist and dry air and for room temperature and 200°C. We used the values of β_e measured with the ion chamber with two different dose-rate regions (front and back) and predicted the equilibrium field. An iterative procedure, like that for the ion chamber analysis, was needed because of the field dependent quantitites (α, μ, β_e) involved in calculating E_s. For the

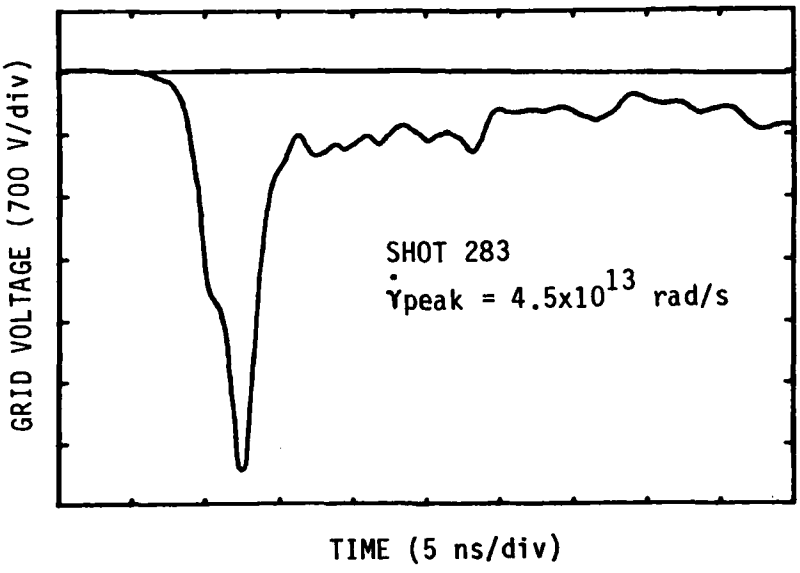

(a)

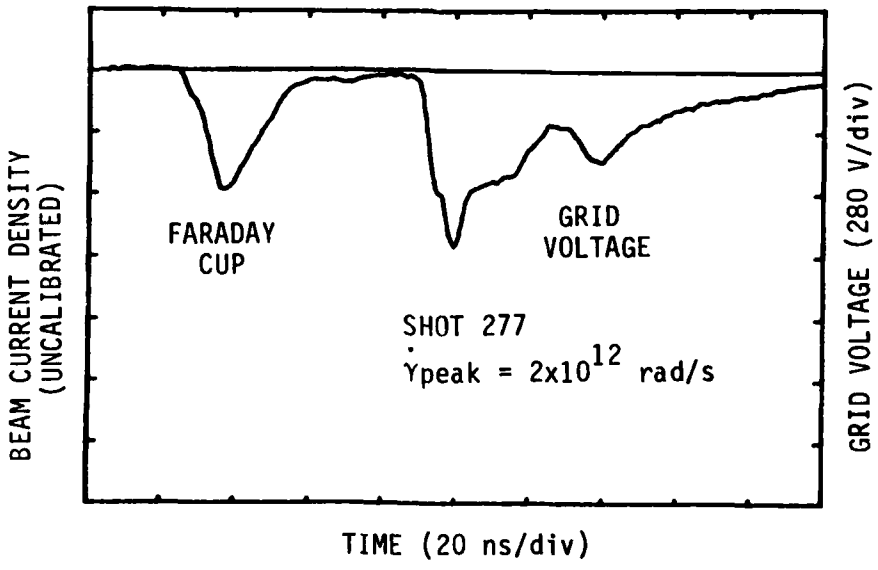

(b)

Figure 21. Waveforms from the equilibrium field diode.

lower dose rate the field is determined mostly by attachment. Our predicted value is 950 V/cm, about 20% higher than the measured values in Table 1. At the high dose rate the field is determined mostly by recombination. Our predicted value is 2300 V/cm, about 50% higher than the measured value. If (because of three-body recombination) the value of β_e was 2×10^{-5} cm^3/s the predicted equilibrium field at the high dose would be greater than 7 kV/cm.

Table 1. The measured equilibrium fields.

Shot	$\dot{\gamma}$ (rad/s)	E V/cm	GAS
274	$\approx 1 \times 10^{12}$	840	2.4% H_2O
275	2.2×10^{12}	770	"
276	2.1×10^{12}	740	"
277	2.0×10^{12}	770	"
283	4.5×10^{13}	1700	"
286	5.3×10^{13}	≈1800	"
287	4.4×10^{13}	1300	"
288	4.4×10^{13}	≈2000	2.1% H_2O, 210°C
289	4.9×10^{13}	≈ 800	"
293	4.6×10^{13}	1500	Dry air, 200°C

The high temperature measurements were very uncertain and it is not possible to tell if there was a change in the equilibrium field. Since the temperature effect of interest involves three-body recombination and we have convincing evidence that there is little of the three-body process operating at these fields, we would not expect to see large changes in the equilibrium field.

SECTION 4
CONCLUSIONS

This experiment shows that, with careful design, large ionization can be produced and measured in an ion chamber using a high current electron beam. Magnetic coupling can be kept to a minimum by keeping the beam diameter small and the current return path close. A field proportional to the derivative of the beam current due to the finite relaxation time of the charge injected into the chamber is the largest perturbation caused by the electron beam. This makes it important to try to keep the current waveform smooth without an excessively fast risetime.

It was also shown that very large current densities can be measured with an ion chamber. The boundary layer did not consume the whole applied voltage. A significant amount of the voltage appeared on the boundary layer, but sufficient fields remained in the bulk of the gas. Boundary layer instabilities did not result in breakdown occurring between the cathode and anode of the chamber.

Both the ion chamber measurement of the electron-ion recombination coefficient and the measurement of the equilibrium field show that three-body recombination is not a significant electron removal process at EMP fields.

SECTION 5
LIST OF REFERENCES

1. Gorbics, S.G., F. H. Attix, and K. Kerris, "Thermoluminescent Dosimeters for High-Dose Applications", Health Phys. 25, 499 (1973).

2. Graybill, S.E., "Aurora Electron Beam Modification", HDL-TR-1862, Harry Diamond Laboratories, Adelphi, MD, July 1978.

3. King, G.W., Spectroscopy and Molecular Structure, Holt, Rinehart, and Winston, New York, 1964.

4. Littlewood, I.M., M.C. Cornell, B.K. Clark, and K.J. Nygaard, "Two- and Three- Body Electron-Ion Recombination in Carbon Dioxide", J. Phys. D 16, 2113, (1983).

5. Scheibe, M., private communication, Mission Research Corporation, Santa Barbara, CA.

6. Sennhauser, E.S., D.A. Armstrong, and J.M. Warman, "The Temperature Dependence of Three-Body Electron Ion Recombination in Gaseous H_2O, NH_3, and CO_2", Radiat. Phys. Chem., 15, 479 (1980).

7. van Lint, V.A.J., "Electron Mobility and Attachment in Dry and Moist Air", Defense Nuclear Agency, DNA 6109T, April 1982.

8. Warman, J.M., E.S. Sennhauser, and D.A. Armstrong, "Three-Body Electron-Ion Recombination in Molecular Gases", J. Chem. Phys. 70, 995, (1979).

DISTRIBUTION LIST

DEPARTMENT OF DEFENSE

ARMED FORCES STAFF COLLEGE
ATTN: LIBRARY

ASSIST SECY OF DEF CMD, CONT, COMM & INTEL
ATTN: ASSISTANT DIRECTOR (SYS)
ATTN: ASSISTANT FOR NATO C3
ATTN: C3 SYSTEMS
ATTN: DADSD(I)
ATTN: PROGRAMS & RESOURCES
ATTN: STRAT C3 SYSTEM
ATTN: TACTICAL INTELLIGENCE SYS
ATTN: TELECOMM SYSTEMS

ASSISTANT SECRETARY OF DEFENSE
ATTN: DEP ASST SECY PROG DEV

ASSISTANT TO THE SECRETARY OF DEFENSE
ATTN: C3I
ATTN: EXECUTIVE ASSISTANT

COMMANDER IN CHIEF, ATLANTIC
ATTN: J5

COMMANDER IN CHIEF, PACIFIC
ATTN: C3SRD

DEFENSE COMMUNICATIONS AGENCY
ATTN: C313

DEFENSE COMMUNICATIONS AGENCY
ATTN: COMMANDER

DEFENSE COMMUNICATIONS ENGINEER CENTER
ATTN: CODE R123 TECH LIB
ATTN: CODE R400
ATTN: CODE R720

DEFENSE INTELLIGENCE AGENCY
ATTN: DT SCI-TECH INTELL
ATTN: RTS-2A TECH LIB
ATTN: RTS-2B

DEFENSE NUCLEAR AGENCY
ATTN: RAAE
ATTN: RAEE
ATTN: RAEV
ATTN: STNA
ATTN: STRA
ATTN: STSP
4 CYS ATTN: STTI-CA

DEFENSE TECHNICAL INFORMATION CENTER
12 CYS ATTN: DD

FIELD COMMAND, DNA, DET 2
LAWRENCE LIVERMORE NATIONAL LABORATORY
ATTN: FC-1

FIELD COMMAND, DEFENSE NUCLEAR AGENCY
ATTN: FCLMC F LEHR

DNA PACOM LIAISON OFFICE
ATTN: DNA LNO
ATTN: DNA LNO

INTERSERVICE NUCLEAR WEAPONS SCHOOL
ATTN: TTV

JOINT CHIEFS OF STAFF
ATTN: C3S EVALUATION OFFICE (HDOO)
ATTN: GD10 J-5 NUC & CHEM DIV
ATTN: J-3 NUCLEAR CONTINGENCY BRANCH
ATTN: J-3 STRATEGIC OPERATIONS DIVISION
ATTN: J-3 WWMCCS & TELECOMMUNICATIONS
ATTN: SAGA

JOINT STRAT TGT PLANNING STAFF
ATTN: JLAA
ATTN: JLK ATTN: DNA REP
ATTN: JLKC
ATTN: JLKS
ATTN: JPPFA
ATTN: JPPFD
ATTN: JPSS
ATTN: JPTM

JOINT TACTICAL C3 AGENCY
ATTN: C3A-ARJS
ATTN: C3A-SES

NATIONAL COMMUNICATIONS SYSTEM
ATTN: NCS-TS

NATIONAL DEFENSE UNIVERSITY
ATTN: NWCLB-CR

NATIONAL SECURITY AGENCY
ATTN: CHIEF A GROUP

OFFICE OF THE SEC OF DEFENSE
ATTN: DOCUMENT CONTROL

PROGRAM ANALYSIS & EVALUATION
ATTN: GENERAL PURPOSE PROGRAMS

U S EUROPEAN COMMAND
ATTN: ECC35-CC

U S FORCES KOREA
ATTN: CJ-P-G
ATTN: DJ-AM-SM

U S NATIONAL MILITARY REPRESENTATIVE
ATTN: U S DOCUMENTS OFFICER

UNDER SECY OF DEF FOR RSCH & ENGRG
ATTN: DEPUNDSEC COM SYS
ATTN: DEPUNDSEC C3I-STRATEGIC & C2 SYS
ATTN: STRAT & SPACE SYS(OS)
ATTN: STRAT & THEATER NUC FOR. F VAJDA
ATTN: TACTICAL WARFARE PROG

DEPARTMENT OF THE ARMY

BMD ADVANCED TECHNOLOGY CENTER
ATTN: ATC-R
ATTN: ATC-T

BMD PROGRAM OFFICE
ATTN: DACS-BM J KAHLAS 13101

BMD SYSTEMS COMMAND
ATTN: BMDSC-HW

DEFENSE COMMUNICATIONS SYSTEMS
ATTN: DRCPM-COM-W-D

DEP CH OF STAFF FOR OPS & PLANS
ATTN: DAMO-ODW

DEP CH OF STAFF FOR RSCH DEV & ACQ
ATTN: DAMA-CSS-N

HARRY DIAMOND LABORATORIES
ATTN: CHIEF DIV 10000
ATTN: DELHD-NW
ATTN: DELHD-NW-EA 21100
ATTN: DELHD-TA-L 81100 TECH LIB
ATTN: DELHD-TF
ATTN: SLCHD-NE-EB
ATTN: SLCHD-NW-ED
ATTN: SLCHD-NW-EE
ATTN: SLCHD-NW-P
ATTN: SLCHD-NW-R
ATTN: SLCHD-NW-RA
ATTN: SLCHD-NW-RC
ATTN: SLCHD-NW-RH G MERKEL
ATTN: SLCHD-NW-RH R GILBERT 22800
ATTN: SLCHD-NW-RI G HUTTLIN
2 CYS ATTN: SLHHD-NW-E

DEPARTMENT OF THE ARMY HEADQUARTERS
ATTN: DAMO-TCV-A

JOINT MANAGEMENT OFFICE
ATTN: JMO-TCS

RESEARCH & DEV CENTER
ATTN: DRCPM-ATC
ATTN: DRCPM-TDS-SD

U S ARMY ARMOR CENTER
ATTN: TECHNICAL LIBRARY

U S ARMY ARMOSPHERIC SCIENCES LAB
ATTN: DELAS-AS

U S ARMY BALLISTIC RESEARCH LAB
ATTN: CAL
ATTN: DRDAR-BLA-S TECH LIB
ATTN: DRDAR-BLE
ATTN: DRDAR-BLV
ATTN: TBL

U S ARMY COMB ARMS COMBAT DEV ACTY
ATTN: ATZL-CAC-A
ATTN: ATZL-CAN-I
ATTN: ATZL-CAP

U S ARMY COMD & GENERAL STAFF COLLEGE
ATTN: LIBRARY

U S ARMY COMM-ELEC ENGRG INSTAL AGENCY
ATTN: CCC-CED-SES

U S ARMY COMMUNICATIONS SYS AGENCY
ATTN: CCM-AD-LB LIBRARY

U S ARMY CONCEPTS ANALYSIS AGENCY
ATTN: CODE 605/606

U S ARMY ENGINEER DIV HUNTSVILLE
ATTN: HNDED-SR

U S ARMY INFORMATION SYSTEMS CMD
ATTN: AS-PLNS-S
ATTN: CC-ENGR
ATTN: CC-OPS-OS
ATTN: CC-OPS-WR

U S ARMY INTELLIGENCE CENTER & SCHOOL
ATTN: ATSI-CD-MD

U S ARMY MATERIAL COMMAND
ATTN: DRXAM-TL TECH LIB

U S ARMY MATERIEL SYS ANALYSIS ACTVY
ATTN: DRXSY-CC
ATTN: DRXSY-DS
ATTN: DRXSY-PO
ATTN: DRXSY-S

U S ARMY MOBILITY EQUIP R&D CMD
ATTN: DRDME-WC TECH LIB

U S ARMY NUCLEAR & CHEMICAL AGENCY
ATTN: LIBRARY

U S ARMY TEST AND EVALUATION COMD
ATTN: TECHNICAL LIBRARY

U S ARMY TRADOC SYS ANALYSIS ACTVY
ATTN: ATAA-TAC

U S ARMY TRAINING AND DOCTRINE COMD
ATTN: ATCD-Z
ATTN: TECHNICAL LIBRARY

U S ARMY WAR COLLEGE
ATTN: LIBRARY

USA MISSILE COMMAND
ATTN: AMSMI-SF
ATTN: DOCUMENTS SECTION
ATTN: DRCPM-PE-EA
ATTN: DRCPM-PE-EG
ATTN: DRSMI-RGP

DEPARTMENT OF THE NAVY

NAVAL AIR SYSTEMS COMMAND
ATTN: AIR 350F
ATTN: AIR 5161

NAVAL FACILITIES ENGINEERING COMMAND
ATTN: 04E

DEPARTMENT OF THE NAVY (CONTINUED)

NAVAL INTELLIGENCE SUPPORT CTR
ATTN: NISC-45

NAVAL OCEAN SYSTEMS CENTER
ATTN: CODE 4471 TECH LIB

NAVAL ORDNANCE STATION
ATTN: STANDARDIZATION DIVISION

NAVAL POSTGRADUATE SCHOOL
ATTN: CODE 1424 LIBRARY

NAVAL RESEARCH LABORATORY
ATTN: CODE 2627 TECH LIB

NAVAL SURFACE WEAPONS CENTER
ATTN: CODE F30
ATTN: CODE F32
ATTN: CODE H20
ATTN: CODE R40
ATTN: CODE R43
ATTN: CODE 425

NAVAL SURFACE WEAPONS CENTER
ATTN: CODE F-56

NAVAL TELECOMMUNICATIONS COMMAND
ATTN: DEPUTY DIRECTOR SYSTEMS

NAVAL WEAPONS CENTER
ATTN: CODE 343 FKA6A2 TECH SVCS

OFC OF THE DEPUTY CHIEF OF NAVAL OPS
ATTN: NOP 098 OFC RES-DEV-TEST & EVAL
ATTN: NOP 506
ATTN: NOP 551
ATTN: NOP 654 STRAT EVAL & ANAL BR
ATTN: NOP 94
ATTN: NOP 981
ATTN: NOP 981N1

OFFICE OF NAVAL RESEARCH
ATTN: CODE 427

SPACE & NAVAL WARFARE SYSTEMS CMD
ATTN: PME 117-21
ATTN: TECHNICAL LIBRARY

STRATEGIC SYSTEMS PROGRAMS(PM-1)
ATTN: NSP-43 TECH LIB

THEATER NUCLEAR WARFARE PROGRAM OFC
ATTN: PMS 423

U S NAVAL FORCES, EUROPE
ATTN: N54

DEPARTMENT OF THE AIR FORCE

AERONAUTICAL SYSTEMS DIVISION, AFSC
ATTN: ASD/ENESS P MARTH
ATTN: ASD/ENSSA
ATTN: ASD/YYEF

AEROSPACE DEFENSE COMMAND
ATTN: ADCOM/J2A
ATTN: J6T

AIR FORCE/INE
ATTN: INA

AIR FORCE AERONAUTICAL SYS DIV
ATTN: AFWAL/FIEA
ATTN: ASD/ENACE

AIR FORCE COMMUNICATIONS COMMAND
ATTN: SIM/SA

AIR FORCE GEOPHYSICS LABORATORY
ATTN: SULL

AIR FORCE INSTITUTE OF TECHNOLOGY
ATTN: LIBRARY

AIR FORCE WEAPONS LABORATORY, AFSC
ATTN: NAT
ATTN: NT
ATTN: NTAEE
ATTN: NTYC
ATTN: NTYE
ATTN: NTYEE
ATTN: NTYEP
ATTN: SUL

AIR LOGISTICS COMMAND
ATTN: OO-ALC/MM
ATTN: OO-ALC/MMETH
ATTN: OO-ALC/MMETH

AIR UNIVERSITY LIBRARY
ATTN: AUL-LSE

ASSISTANT CHIEF OF STAFF
ATTN: AF/SAMI TECH INFO DIV

BALLISTIC MISSILE OFFICE/DAA
ATTN: ENSN

DEPUTY CHIEF OF STAFF
ATTN: LEEEU

DEPUTY CHIEF OF STAFF
ATTN: AF/RDQI

DEPUTY CHIEF OF STAFF
ATTN: AFRDS SPACE SYS & C3 DIR

DEPUTY CHIEF OF STAFF
ATTN: AFXOXFM PLNS, FRC DEV MUN PLNS

ELECTRONIC SYSTEMS DIVISION
ATTN: SCS-1E

FOREIGN TECHNOLOGY DIVISION, AFSC
ATTN: NIIS LIBRARY

UNITED STATES AIR FORCE HEADQUARTERS
ATTN: SAS

DEPARTMENT OF THE AIR FORCE (CONTINUED)

NORAD
ATTN: NORAD/J5YX

ROME AIR DEVELOPMENT CENTER, AFSC
ATTN: TSLD

SPACE COMMAND
ATTN: DEE

SPACE DIVISION
ATTN: IND

SPACE DIVISION
ATTN: YKM

STRATEGIC AIR COMMAND
ATTN: DEMUE

STRATEGIC AIR COMMAND
ATTN: DEPR

STRATEGIC AIR COMMAND
ATTN: DOCSD

STRATEGIC AIR COMMAND
ATTN: INAD

STRATEGIC AIR COMMAND
ATTN: INAO

STRATEGIC AIR COMMAND
ATTN: SAC/LGW

STRATEGIC AIR COMMAND
ATTN: NRI/STINFO

STRATEGIC AIR COMMAND
ATTN: SAC/SIP

STRATEGIC AIR COMMAND
ATTN: XPFC

STRATEGIC AIR COMMAND
ATTN: XPFR

STRATEGIC AIR COMMAND
ATTN: XPFS

STRATEGIC AIR COMMAND
ATTN: XPQ

TACTICAL AIR COMMAND
ATTN: TAC/XPJ

U S AIR FORCES IN EUROPE
ATTN: USAFE/XPXX

U S RESEARCH & DEVELOPMENT COORD
ATTN: USRADCO

DEPARTMENT OF ENERGY

EMERGENCY ELECTRIC POWER ADM
ATTN: LIBRARY

UNIVERSITY OF CALIFORNIA
LAWRENCE LIVERMORE NATIONAL LAB
ATTN: L-658 TECH INFO DEPT LIB

LOS ALAMOS NATIONAL LABORATORY
ATTN: MS P364 REPORTS LIBRARY

SANDIA NATIONAL LABORATORIES
ATTN: TECH LIB 3141

OTHER GOVERNMENT

CENTRAL INTELLIGENCE AGENCY
ATTN: OSR/SE/C
ATTN: OSR/SE/F
ATTN: OSWR/NED
ATTN: OSWR/STD/MTB

FEDERAL EMERGENCYS MANAGEMENT AGENCY
ATTN: SL-EM

NATIONAL BUREAU OF STANDARDS
ATTN: 723.03

DEPARTMENT OF DEFENSE CONTRACTORS

AEROSPACE CORP
ATTN: LIBRARY

AGBABIAN ASSOCIATES, INC
ATTN: LIBRARY

ALLIED CORP
ATTN: DOCUMENT CONTROL

ALLIED CORP
ATTN: DEPT 6401

AT&T TECHNOLOGIES, INC
ATTN: W EDWARDS

AVCO SYSTEMS DIVISION
ATTN: LIBRARY A830

BDM CORP
ATTN: CORPORATE LIB

BDM CORP
ATTN: LIBRARY

BOEING CO
ATTN: D EGELKROUT
ATTN: D KEMLE
ATTN: H WICKLEIN
ATTN: KENT TECHNICAL LIBRARY
ATTN: ORG 2-3744
ATTN: R SCHEPPE

DEPARTMENT OF DEFENSE CONTRACTORS (CONTINUED)

BOEING MILITARY AIRPLANE CO
ATTN: C SUTTER

BOOZ-ALLEN & HAMILTON, INC
ATTN: TECHNICAL LIBRARY

BOOZ-ALLEN & HAMILTON, INC
ATTN: L ALBRIGHT

BOOZ-ALLEN & HAMILTON, INC
ATTN: D DURGIN

CALSPAN CORP
ATTN: LIBRARY

COMPUTER SCIENCES CORP
ATTN: A SCHIFF

DIKEWOOD CORP
ATTN: TECHNICAL LIBRARY

DIKEWOOD CORP
ATTN: K LEE

E-SYSTEMS, INC
ATTN: E WILKES

E-SYSTEMS, INC
ATTN: J MOORE

EG&G WASH ANALYTICAL SVCS CTR, INC
ATTN: A BONHAM
ATTN: C GILES

ELECTRO-MAGNETIC APPLICATIONS, INC
ATTN: D MEREWETHER

FORD AEROSPACE & COMMUNICATIONS CORP
ATTN: H LINDER

GENERAL ELECTRIC CO
ATTN: C HEWISON

GRUMMAN AEROSPACE CORP
ATTN: L-01 35

HARRIS CORP
ATTN: V PRES & MGR PRGMS DIV

HERCULES, INC
ATTN: W WOODRUFF

HONEYWELL, INC
ATTN: S&RC LIBRARY

HONEYWELL, INC
ATTN: LIBRARY

HUGHES AIRCRAFT CO
ATTN: CTD 6

IIT RESEARCH INSTITUTE
ATTN: I MINDEL

INSTITUTE FOR DEFENSE ANALYSES
ATTN: CLASSIFIED LIBRARY
ATTN: TECH INFO SERVICES

IRT CORP
ATTN: B WILLIAMS
ATTN: R W STEWART

ITT TELECOMMUNICATIONS CORP
ATTN: R SCHWALLIE

JAYCOR
ATTN: E WENAAS

JAYCOR
ATTN: LIBRARY

JOHNS HOPKINS UNIVERSITY
ATTN: P PARTRIDGE

KAMAN SCIENCES CORP
ATTN: LIBRARY

KAMAN SCIENCES CORP
ATTN: E CONRAD

KAMAN TEMPO
ATTN: DASIAC
ATTN: R RUTHERFORD

KAMAN TEMPO
ATTN: DASIAC

LITTON SYSTEMS, INC
ATTN: E EUSTIS

LITTON SYSTEMS, INC
ATTN: J MOYER

LITTON SYSTEMS, INC
ATTN: J SKAGGS

LOCKHEED MISSILES & SPACE CO, INC
ATTN: TECH INFO CTR D/COLL, D/90-11, B/106

LTV AEROSPACE & DEFENSE COMPANY
ATTN: 2-58010 LIBRARY

LUTECH, INC
ATTN: F TESCHE

MCDONNELL DOUGLAS CORP
ATTN: TECHNICAL LIBRARY SERVICES

MCDONNELL DOUGLAS CORP
ATTN: TECHNICAL LIBRARY

METATECH CORP
ATTN: R SCHAEFER

METATECH CORPORATION
ATTN: W RADASKY

MISSION RESEARCH CORP
ATTN: EMP GROUP

DEPARTMENT OF DEFENSE CONTRACTORS (CONTINUED)

MISSION RESEARCH CORP
ATTN: J LUBELL

MISSION RESEARCH CORP, SAN DIEGO
2 CYS ATTN: J CHERVENAK
2 CYS ATTN: V VAN LINT

MITRE CORP
ATTN: M FITZGERALD

PACIFIC-SIERRA RESEARCH CORP
ATTN: H BRODE, CHAIRMAN SAGE

PHYSICS INTERNATIONAL CO
ATTN: DOCUMENT CONTROL

R & D ASSOCIATES
ATTN: DOCUMENT CONTROL
ATTN: P HAAS
ATTN: W KARZAS

R & D ASSOCIATES
ATTN: LIBRARY

RAYTHEON CO
ATTN: H FLESCHER

RCA CORP
ATTN: G BRUCKER

RESEARCH TRIANGLE INSTITUTE
ATTN: M SIMONS

ROCKWELL INTERNATIONAL CORP
ATTN: G MORGAN D256/MC BA36
ATTN: J ERB D257/MC BB17

ROCKWELL INTERNATIONAL CORP
ATTN: B-1 DIV TIC BA0B

S-CUBED
ATTN: A WILSON

SCIENCE & ENGRG ASSOCIATES, INC
ATTN: V JONES

SCIENCE APPLICATIONS INTL CORP
ATTN: W CHADSEY

SCIENCE APPLICATIONS, INC
ATTN: E ODONNELL
ATTN: TECH INFO CTR

SPERRY CORP
ATTN: R LAZARCHIK

SPERRY CORP
ATTN: J INDA

SPERRY CORP
ATTN: TECHNICAL LIBRARY

SRI INTERNATIONAL
ATTN: A PADGETT

TELEDYNE BROWN ENGINEERING
ATTN: F LEOPARD

TEXAS INSTRUMENTS, INC
ATTN: TECHNICAL LIBRARY

TRW ELECTRONICS & DEFENSE SECTOR
ATTN: J BROSSIER
ATTN: J PENAR

TRW ELECTRONICS & DEFENSE SECTOR
ATTN: R HENDRICKSON

TRW ELECTRONICS & DEFENSE SECTOR
ATTN: LIBRARIAN

END

DTIC

5-86